FACULDADE DE ENGENHARIA DA UNIVERSIDADE DO PORTO

Design and Simulation of a Magnetorquer-Based Attitude Control Algorithm for the ICARUS 1U CubeSat

José Serôdio Canha

Mestrado em Engenharia Eletrotécnica e de Computadores

Supervisor: Prof. António Pedro Rodrigues Aguiar

July 31, 2026

Design and Simulation of a Magnetorquer-Based Attitude Control Algorithm for the ICARUS 1U CubeSat

José Serôdio Canha

Mestrado em Engenharia Eletrotécnica e de Computadores

Approved in oral examination by the committee:

President: Prof. Paulo Jorge de Azevedo Lopes dos Santos

Referee: Prof. João Paulo Lopes Monteiro

Referee: Prof. António Pedro Rodrigues Aguiar

July 31, 2026

Resumo

O crescente interesse em missões espaciais de baixo custo e reduzidas dimensões tem impulsionado a adoção generalizada de CubeSats, cujas restrições rigorosas de massa, volume, consumo de energia e recursos computacionais influenciam significativamente o projeto dos seus subsistemas. Entre estes subsistemas, o Attitude Determination and Control System (ADCS) constitui um desafio particularmente exigente, sobretudo quando se recorre exclusivamente à atuação magnética. Os magnetorquers representam uma solução leve, económica e fiável, mas a sua dependência do campo geomagnético local resulta num sistema subatuado em cada instante, dificultando a obtenção de um desempenho de apontamento preciso.

O ICARUS é um CubeSat de 1U em desenvolvimento pela Porto Space Team, no âmbito da iniciativa CubeSat Portugal, com o objetivo de realizar medições in situ do plasma ionosférico. Estes objetivos da missão impõem requisitos rigorosos de atitude, nomeadamente a manutenção de uma precisão de apontamento de $\pm 10^\circ$ relativamente à direção de avanço (ram direction), numa plataforma sujeita a severas limitações de massa, volume e potência disponível. A satisfação destes requisitos recorrendo apenas à atuação por magnetorquers motiva o desenvolvimento de estratégias de controlo simultaneamente robustas e computacionalmente eficientes.

Nesta dissertação é apresentado o desenvolvimento, implementação e validação numérica de uma arquitetura de controlo de atitude adaptada à missão ICARUS. É formulada uma lei de controlo "*sliding mode*" não linear em coordenadas de erro por quaterniões, de forma a lidar explicitamente com as não linearidades do sistema e com as suas restrições de atuação variantes no tempo. O controlador proposto é integrado num ambiente de simulação de elevada fidelidade, que modela a dinâmica orbital, as variações do campo geomagnético e o comportamento rotacional do satélite. Para efeitos de comparação, é igualmente implementada uma lei de controlo proporcional derivativa baseada em quaterniões, permitindo uma avaliação sistemática do desempenho de ambas as abordagens.

O desempenho dos dois controladores é avaliado através de simulações de Monte Carlo em cenários de apontamento estático e dinâmico representativos das condições da missão. Os resultados demonstram que o "*sliding mode*" atinge um erro médio de apontamento de aproximadamente 5°, satisfazendo de forma consistente o requisito da missão, enquanto o controlador proporcional derivativo apresenta erros em regime permanente superiores a 20° nas mesmas condições.

Estes resultados demonstram que o controlo de atitude baseado exclusivamente em magnetorquers pode satisfazer requisitos moderados de apontamento quando são empregues estratégias de controlo não lineares adequadas. O principal contributo deste trabalho reside no desenvolvimento e validação de uma abordagem de controlo robusta que melhora significativamente a precisão de apontamento relativamente aos métodos clássicos, mantendo simultaneamente a compatibilidade com as limitações computacionais e energéticas inerentes a uma plataforma CubeSat de 1U.

Abstract

The increasing interest in low cost and compact space missions has driven the widespread adoption of CubeSats, where strict constraints on mass, volume, power consumption, and computational resources significantly influence subsystem design. Among these subsystems, the Attitude Determination and Control System (ADCS) represents a critical challenge, particularly when relying exclusively on magnetic actuation. Magnetorquers provide a lightweight, low cost, and reliable solution, but their dependence on the local geomagnetic field leads to an underactuated system at any instant in time, which complicates the achievement of accurate pointing performance.

ICARUS is a 1U CubeSat under development by the Porto Space Team within the CubeSat Portugal initiative, aimed at performing in situ ionospheric plasma measurements. These mission objectives impose stringent attitude requirements, namely maintaining a pointing accuracy of $\pm 10^\circ$ relative to the ram direction, on a platform subject to severe limitations in mass, volume, and available power. Addressing this requirement with magnetorquer only actuation motivates the development of control strategies that are both robust and computationally efficient.

This thesis presents the design, implementation, and numerical validation of an attitude control framework tailored to the ICARUS mission. A nonlinear sliding mode control law is formulated in quaternion error coordinates to explicitly address the system nonlinearities and its time varying actuation constraints. The proposed controller is integrated into a high fidelity simulation environment that captures orbital dynamics, geomagnetic field variations, and spacecraft rotational behavior. For comparison purposes, a classical quaternion based Proportional Derivative (PD) control law is also implemented within the same framework, enabling a systematic performance assessment.

The performance of both controllers is evaluated through Monte Carlo simulations under static and dynamic pointing scenarios representative of mission conditions. The results show that the sliding mode controller achieves an average pointing error of approximately 5°, consistently satisfying the mission requirement, while the PD controller exhibits steady state errors exceeding 20° under identical conditions.

These results demonstrate that magnetorquer only attitude control can meet moderate pointing requirements when appropriate nonlinear control strategies are employed. The main contribution of this work lies in the development and validation of a robust control approach that significantly improves pointing accuracy over classical methods while remaining compatible with the computational and power limitations of a 1U CubeSat platform.

Contents

1 Introduction **1**
1.1 Objectives . . . 2
1.2 Main Contributions . . . 3
1.3 Structure of the Document . . . 4

2 ICARUS **5**
2.1 Spacecraft Architecture and Subsystems . . . 5
2.1.1 Langmuir Probe and Plasma Measurement Principles . . . 6
2.1.2 Attitude Determination and Control System . . . 7
2.1.3 Magnetorquer Design and Actuation Principles . . . 8

3 Background **10**
3.1 Orbital Dynamics and Mission Orbit . . . 10
3.1.1 Fundamentals of Orbital Mechanics . . . 10
3.1.2 ICARUS Orbit Selection and Parameters . . . 12
3.1.3 Orbit Propagation and Simulation Methods . . . 12
3.2 Attitude Dynamics and Control Modeling . . . 13
3.2.1 Reference Frames for Spacecraft Attitude Representation . . . 13
3.2.2 Attitude Representation and State Space Formulation . . . 15

4 Magnetic Attitude Control Methods **18**
4.1 Overview of Magnetic Attitude Control Techniques . . . 18
4.2 Classical Control Approaches for Magnetorquer Systems . . . 19
4.2.1 B-dot Detumbling Algorithm . . . 19
4.2.2 Quaternion Based Proportional Derivative Control . . . 20
4.3 Sliding Mode Control for Magnetically Actuated Spacecraft . . . 21

5 Simulation Framework and Performance Evaluation **24**
5.1 Simulation Framework . . . 24
5.1.1 Overview of the Simulation Architecture . . . 24
5.1.2 Orbital and Environmental Modeling . . . 26
5.1.3 Control Implementation . . . 26
5.1.4 Spacecraft Dynamics and Numerical Integration . . . 28
5.1.5 Simulation Setup and Performance Metrics . . . 28
5.2 Performance Evaluation . . . 28
5.2.1 B-dot Algorithm Detumble Performance . . . 29
5.2.2 Static Target Pointing Performance . . . 31
5.2.3 Dynamic Target Tracking Performance . . . 35

5.2.4 Power Consumption Analysis 41
5.2.5 Overall Discussion and Simulation Limitations 45

6 Conclusion **46**

References **48**

List of Figures

1.1 ICARUS Satellite Concept Art. 1

2.1 ICARUS' System Configuration 5
2.2 Representative I –V curve for a Langmuir probe [4]. 6
2.3 Control circuit. 8
2.4 Z- coil Printed Circuit Board (PCB) design. 9

3.1 Orbital Parameters[11] 11
3.2 Spacecraft Body Frame 13
3.3 Earth Centred Inertial (ECI)[14] 14
3.4 Orbital reference frame[15] 15

5.1 Simulator single iteration flowchart 25
5.2 Simulator render of ICARUS 25
5.3 Sliding mode quaternion response to dynamic target without low-pass filter: attitude quaternion(blue) and target quaternion (orange) 27
5.4 Sliding mode quaternion response to dynamic target with low-pass filter: attitude quaternion(blue) and target quaternion (orange) 27
5.5 B-dot control law: average angular velocity for $20^{\circ}/s$ initial angular velocity . . . 29
5.6 B-dot control law: average angular velocity for $80^{\circ}/s$ initial angular velocity . . . 30
5.7 B-dot control law: average angular velocity for $240^{\circ}/s$ initial angular velocity . . 30
5.8 PD control law: average attitude error quaternion for a static target 31
5.9 Sliding mode control law: average attitude error quaternion for a static target . . 32
5.10 PD control law: average Euler-angle attitude error for a static target 32
5.11 Sliding mode control law: average Euler-angle attitude error for a static target . . 33
5.12 PD control law: average error angular velocity for a static target 34
5.13 Sliding mode control law: average error angular velocity for a static target 34
5.14 PD control law: average attitude quaternion (blue) and dynamic target quaternion (orange) 36
5.15 Sliding mode control law: average attitude quaternion (blue) and dynamic target quaternion (orange) 36
5.16 PD control law: average Euler-angle attitude error for a dynamic target 37
5.17 Sliding mode control law: average Euler-angle attitude error for a dynamic target 38
5.18 PD control law: average angular velocity (blue) and target angular velocity (orange) 39
5.19 PD control law: average error angular velocity for dynamic target 39
5.20 Sliding mode control law: average angular velocity (blue) and target angular velocity (orange) 40
5.21 Sliding mode control law: average error angular velocity for dynamic target . . . 40
5.22 Sliding mode control law: power consumption for a dynamic target with $\varepsilon = 3 \times 10^{-3}$ 42

5.23 Sliding mode control law: power consumption for a dynamic target with $\varepsilon = 3.09 \times 10^{-2}$ 42
5.24 Sliding mode control law: Euler-angle attitude error for a dynamic target with $\varepsilon = 3.09 \times 10^{-2}$ 43
5.25 PD control law: average power consumption for a dynamic target 44
5.26 Sliding mode control law: average power consumption for a dynamic target . . . 44

List of Tables

2.1 Attitude determining Sensors Key parameters. 7
2.2 Control Circuit components. 8

3.1 Orbit parameters. 12

5.1 B-dot Simulations values at 4 hours 31
5.2 Static case simulation values at 12 hours 35
5.3 Dynamic target case simulation values at 12 hours 41

List of Acronyms

ADC	Analog-to-Digital Converter
ADCS	Attitude Determination and Control System
DAC	Digital-to-Analog Converter
ECEF	Earth Centred/Earth Fixed
ECI	Earth Centred Inertial
GCI	Geocentric Inertial Frame
ICRF	International Celestial Reference Frame
LDO	Low Dropout Regulator
LEO	Low Earth Orbit
MCU	Microcontroller Unit
MPC	Model Predictive Control
m-NLP	multi-Needle Langmuir Probe
NORAD	North American Aerospace Defense Command
OBC	On-Board-Computer
OML	Orbital Motion Limited
PCB	Printed Circuit Board
PD	Proportional Derivative
PWM	Pulse Width Modulation
RAAN	Right Ascension of the Ascending Node
SGP4	Simplified General Perturbations 4
SSO	Sun-Synchronous Orbit
UGES	Uniformly, Globally Exponentially Stabilizing
TLE	Two-Line Elements
WMM	World Magnetic Model

Chapter 1

Introduction

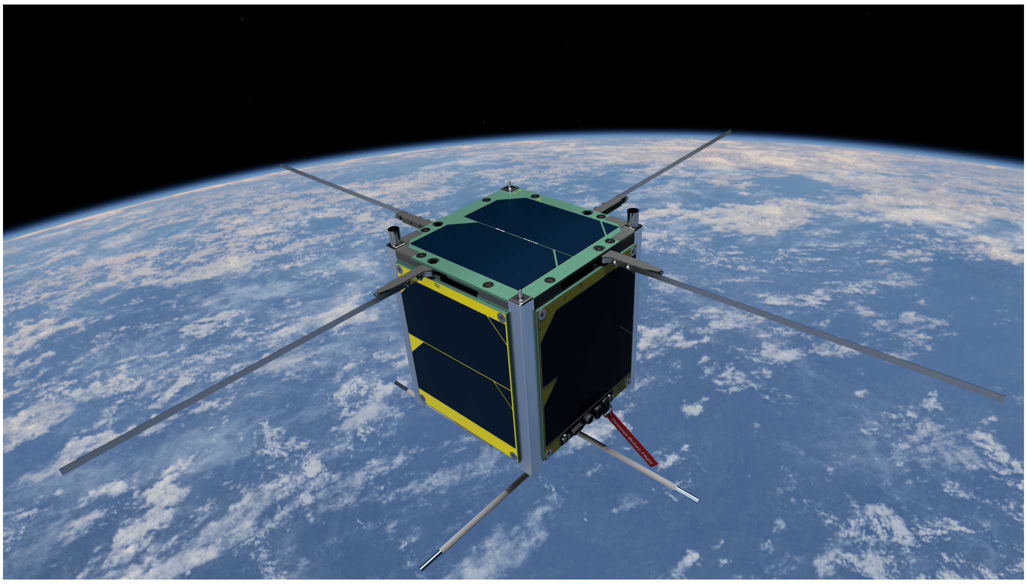

Figure 1.1: ICARUS Satellite Concept Art.

In 2024, the Portugal Space Agency launched the CubeSat Portugal initiative with the objective of fostering satellite development within Portuguese universities. The national competition offers the winning student team the opportunity to launch the developed 1U CubeSat into Low Earth Orbit (LEO), promoting hands-on education and space technology development.

Project ICARUS (Fig. 1.1) is a 1U CubeSat mission proposed by the Porto Space Team [1] within the scope of this initiative. The mission aims to develop, launch, and operate a nano-satellite carrying a miniaturized multi-needle Langmuir probe to measure ionospheric electron density and temperature. These measurements enable high-resolution in-situ characterization of ionospheric plasma dynamics.

The ionosphere is a highly variable region of the Earth's upper atmosphere whose behavior directly affects satellite communications, navigation systems, and space-weather phenomena. Small-scale plasma irregularities, particularly in auroral and high-latitude regions, are known to induce signal scintillation and performance degradation. Despite extensive research, many of these irregularities remain insufficiently characterized due to limited spatial and temporal resolution of existing measurements.

Because the spacecraft body can disturb the surrounding plasma, the Langmuir probe must be oriented as far as possible from the satellite structure. This requirement imposes a stringent attitude control constraint, formalized as

Requirement 1 *ADCS-MR-010:*
The Attitude Determination and Control System (ADCS) shall be capable of pointing the Langmuir probe within $\pm 10^\circ$ *of the ram direction.*

To satisfy this requirement while minimizing system complexity, ICARUS is equipped exclusively with magnetorquer actuators, avoiding reaction wheels and thereby reducing mass, volume, power consumption, and cost. And thus, the main purpose of this thesis will be to design an algorithm capable of controlling this system with the missions necessary accuracy.

Although spacecraft attitude control is a well studied problem, achieving accurate pointing using solely magnetic actuation remains challenging [2]. Magnetorquers inherently generate small control torques due to the low intensity of the Earth's magnetic field, and the resulting torque lies in the plane orthogonal to the geomagnetic field as shown by equation 2.3. Consequently, magnetorquer based attitude control systems are instantaneously underactuated. Nevertheless, such systems are controllable due to the time varying nature of the geomagnetic field, provided that orbital configurations close to the magnetic equator are avoided [3]. Due to this satellites that use of these systems usually perform missions that have low pointing accuracy requirements. Despite their limitations, magnetorquer-only solutions remain highly attractive for small CubeSats and pico satellites due to their simplicity and low resource requirements. Their primary drawback, limited pointing accuracy, motivates continued research into advanced control strategies capable of enhancing performance and enabling more demanding scientific missions on small satellite platforms. More advanced control algorithms provide a potential solution to this limitation. But as nano-satellites are severely constrained in available solar panel area, power budget becomes a critical design factor. As a result, On-Board-Computer (OBC) are typically low-power Microcontroller Unit (MCU), limiting the complexity of deployable control algorithms. Nonetheless great advances have been made in the microchip sphere that are introducing more complex and power efficient chip every year, as such this might cease to be a limitation in the near future.

1.1 Objectives

The primary objective of this thesis is to develop an attitude control solution capable of meeting the ICARUS mission requirements while respecting the strict physical and computational constraints inherent to a 1U CubeSat platform. In particular, the work focuses on achieving reliable pointing performance using exclusively magnetorquer actuators, which introduces significant control limitations due to the system underactuation.

More specifically, the objectives of this work can be summarized as follows:

- Formulate the ICARUS attitude control problem based on mission requirements, with emphasis on the $\pm 10^\circ$ pointing accuracy constraint relative to the ram direction.
- Develop a mathematical model of the spacecraft attitude dynamics, including the effects of magnetic actuation and relevant environmental interactions.
- Design a nonlinear control strategy that is robust to model uncertainties and compatible with limited onboard computational resources.
- Implement the proposed control law within a simulation environment capable of representing realistic orbital and geomagnetic conditions.
- Compare the proposed solution with a classical control approach in order to assess its relative performance in terms of pointing accuracy, robustness, and power consumption.

The overall goal is to determine whether magnetorquer only control can provide sufficient performance for the ICARUS mission and to identify control design strategies that maximize its effectiveness.

1.2 Main Contributions

The main contributions of this thesis lie in the development, adaptation, and validation of an attitude control framework tailored to the specific constraints and requirements of the ICARUS CubeSat mission.

First, a complete formulation of the attitude control problem is presented, explicitly incorporating mission level pointing requirements and the limitations imposed by magnetic actuation. This formulation provides a consistent foundation for controller design and evaluation.

Second, a nonlinear sliding mode control law is designed in quaternion error coordinates and adapted to the magnetorquer only actuation scenario. The proposed approach explicitly accounts for the time varying and underactuated nature of the control input, while maintaining low computational complexity suitable for embedded implementation.

Third, a high fidelity simulation environment is developed to evaluate controller performance under realistic conditions. This framework integrates orbital propagation, geomagnetic field modeling, and spacecraft rotational dynamics enabling systematic testing through Monte Carlo simulations.

Finally, a thorough performance comparison between the proposed sliding mode controller and a classical quaternion based Proportional Derivative (PD) controller is carried out. The results demonstrate a significant improvement in pointing accuracy and robustness, showing that the proposed approach meets mission requirements, while the classical method does not under the same conditions.

Together, these contributions provide a validated control solution for the ICARUS mission and offer insight into the design of efficient attitude control systems for magnetorquer only CubeSat platforms.

1.3 Structure of the Document

This document is organized as follows.

Chapter 2 describes the ICARUS hardware architecture of relevant subsystems in order to better contextualize the problem addressed.

Chapter 3 presents the background necessary to understand the problem addressed in this work. It includes relevant orbital mechanics, and the theoretical foundations of spacecraft attitude dynamics and control.

Chapter 4 reviews the state of the art in magnetic attitude control, with emphasis on control strategies suitable for small satellites. The PD and sliding mode control approaches are introduced and their selection for this work is justified.

Chapter 5 describes the simulation environment developed to evaluate the proposed control algorithms. It details the modeling assumptions, numerical methods, and validation procedures, followed by a presentation and discussion of the simulation results for both static and dynamic pointing scenarios.

Finally, Chapter 6 summarizes the main findings of the thesis, highlights the key conclusions, and outlines possible directions for future work.

Chapter 2

ICARUS

In this chapter a description of ICARUS hardware architecture, from physical configuration of the satellite to description of relevant subsystems shall be presented.

2.1 Spacecraft Architecture and Subsystems

The ICARUS satellite can be divided into five categories, based on its distinct subsystems, being: the payload, the antenna, solar panels, Printed Circuit Board (PCB) stack and chassis. Figure 2.1 shows ICARUS physical configuration and its own body reference frame configuration. The Z+,X+ and Y+ solar panels shall house the magnetorquers embedded in their inner layers. Their format is further discussed in subsection 2.1.3. The Langmuir probes will be deployed in the Z-face.

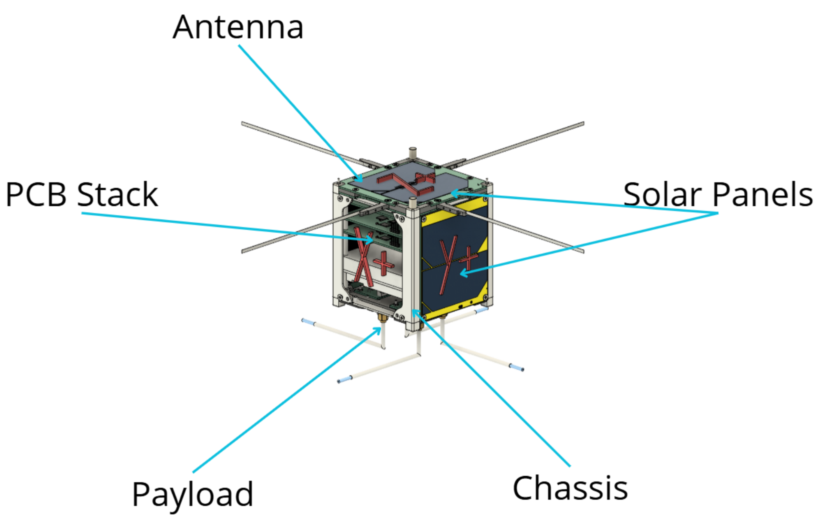

Figure 2.1: ICARUS' System Configuration

It is also important to note that, although considerable effort was made to design the satellite as symmetrically as possible, perfect symmetry is inherently unattainable. Consequently, the inertia matrix contains small off-diagonal terms and is defined as follows:

$$J = \begin{bmatrix} 2.451 \times 10^{-3} & -11426.7032464 \times 10^{-9} & 4452.8279647 \times 10^{-9} \\ -11426.7032464 \times 10^{-9} & 2.406 \times 10^{-3} & 206.8344892 \times 10^{-9} \\ 4452.8279647 \times 10^{-9} & 206.8344892 \times 10^{-9} & 2.154 \times 10^{-3} \end{bmatrix} \tag{2.1}$$

2.1.1 Langmuir Probe and Plasma Measurement Principles

Langmuir probes are recognized as fundamental tools for plasma diagnostics due to their simplicity, versatility, and reliability. These probes help to understand plasma environments and can measure key parameters such as electron temperature, ion temperature, electron density, and plasma potential. Their operational range encompasses a broad spectrum of plasma conditions, including densities, temperatures, and potentials encountered in Earth's ionosphere [4].

The principle of operation is based on the current-voltage (I–V) characteristics derived from the probe's interaction with the surrounding plasma. The Langmuir probe typically operates by inserting an exposed conductor into a plasma, applying a bias relative to the platform potential, and measuring the current collected by the biased probe [5]. By varying the bias voltage, the probe generates an I–V curve that reveals essential plasma properties [4].

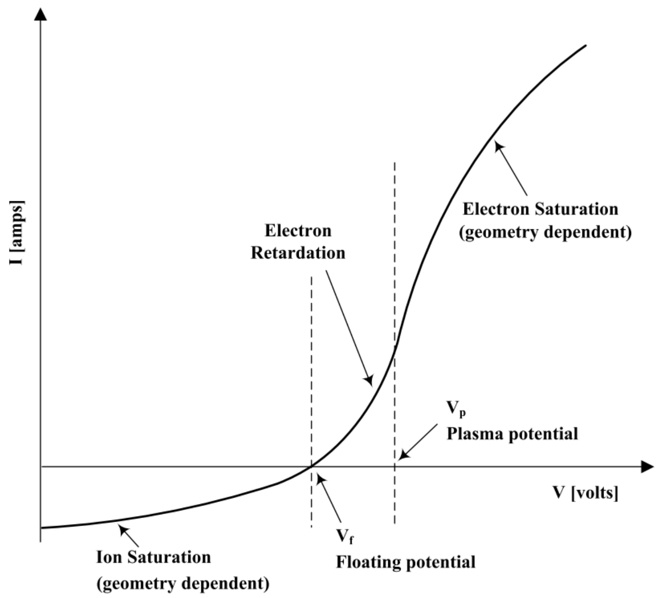

Figure 2.2: Representative I –V curve for a Langmuir probe [4].

The I–V characteristic curve comprises distinct regions, as depicted in Figure 2.2. At highly negative bias voltages, the probe repels electrons, collecting primarily ions and reaching ion saturation current. As the bias voltage increases, it approaches the floating potential, V_f, where electron and ion currents balance. Beyond this point, the plasma potential, V_p, marks the voltage at which electron collection dominates, providing insights into electron density and temperature

[4].

Langmuir probes collect a negative electric current, I, when biased at a positive voltage, V, compared to the surrounding plasma. Mott-Smith and Langmuir derived analytical expressions for this current using what is now known as Orbital Motion Limited (OML) theory [6].

The multi-Needle Langmuir Probe (m-NLP) was first proposed by Jacobsen et al. [7]. This innovative Langmuir probe design utilizing two or more small, fixed-bias cylindrical probes to determine the absolute electron density without requiring knowledge of the electron temperature or spacecraft potential. The only requirement is an estimate of the spacecraft's potential to set the bias values well above it. Each probe is maintained at a distinct potential above the spacecraft potential, and their currents are sampled simultaneously [6].

2.1.2 Attitude Determination and Control System

The ADCS will comprise of the Cortex M33 processor, using the STM32U575 MCU, it will feature the sensors present in the2.1 table, the magnetorquers actuators and its control circuitry.

Table 2.1: Attitude determining Sensors Key parameters.

Type	**Model**	**Power(typ.)**	**Interface**	**RMS Noise**	**Notes**
Gyroscope	BMI323	2.607 mW	I2C/SPI/I3C	0.1661 (°/s)[a]	Redundant Gyro
Gyroscope	I3G4250DTR	20.13 mW	I2C/SPI	0.1061 (°/s)[a]	Primary Gyro
Magnetometer	RM3100	0.693 mW	I2C/SPI	19.596 (nT)[a]	Primary Mag
Magnetometer	IIS2MDCTR	3.729 mW	I2C/SPI	450 (nT)[a]	Redundant Mag
Sun Sensor	Photodiode	1.84 mW	SPI	TBC	Redundant in num.

[a] - The RMS noise are estimations based on data-sheet values and assuming noise is white and normally distributed.

The ICARUS control actuator circuit is based on Ajinkya Phanse's work [8], where current is managed using H-bridge drivers, Low Dropout Regulator (LDO), and a Pulse Width Modulation (PWM) to voltage converter. In ICARUS' version, to optimize redundancy and communication accuracy, the PWM-to-voltage converter is replaced by a Digital-to-Analog Converter (DAC). Current measurement will be handled by shunt resistors and Analog-to-Digital Converter (ADC). Using a resistance in series with the magnetorquer the system will be limiting the maximum output of each actuator to $0.5W$. This way possible malfunctions in space shall not drain the battery instantaneously. The figure 2.3 shows a simplified representation of this circuit using the components in table 2.2.

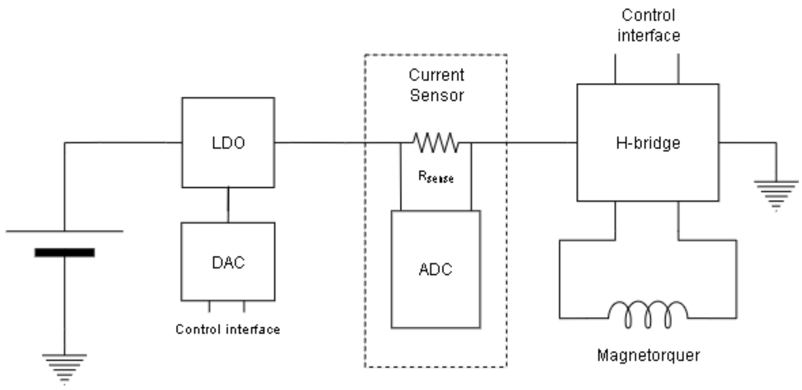

Figure 2.3: Control circuit.

Table 2.2: Control Circuit components.

Type	Model	Power(typ.)	Interface
H-bridge	DRV8212P	36.3 mW	GPIOs
R_{sense}	PRM10	–	GPIOs
LDO	LP2980-ADJ	1.39 mW	GPIOs
ADC	ADS1158	42 mW	SPI/GPIOs
DAC	DAC81404	280.18 mW	SPI

2.1.3 Magnetorquer Design and Actuation Principles

To control a satellite's attitude three options are usually considered in similar projects: thrusters, reaction wheels and magnetorquers. Of the three, magnetic control offers the more compact design and least amount of power budget required. Usual magnetorquer actuators come in either a air-coil or rod formats. Rods are more compact options but require the use of high permeability materials for the core. This increases the weight of the whole system.

A third less common option comes in the form of an air-coil magnetorquer integrated into the inner layer of a PCB [9]. ICARUS' magnetorquer follows this design and has been dimensioned to maximize the available space within the solar panels PCB as shown in figure 2.4 and has the following characteristics:

- Number of PCB layers with coils: $N = 4$
- One coil total area: $A = 0.1698\,m^2$
- One coil resistance: $R_P = 31{,}074\,\Omega$
- Magnetorquer equivalent resistance: $R_i = 7{,}768\,\Omega$
- Consumption limiting resistance: $R_c = 43\,\Omega$
- Magnetorquer maximum magnetic dipole moment: $0.067\,\mathrm{A}m^2$

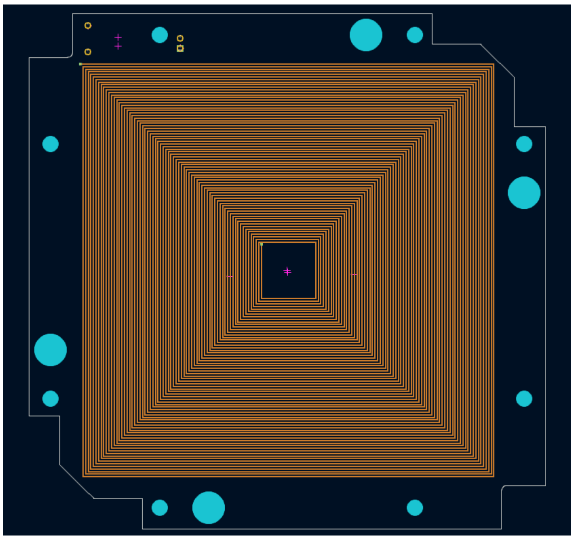

Figure 2.4: Z- coil PCB design.

This design will produce a magnetic moment following

$$m = NAI \tag{2.2}$$

with I being the current that passes through the coil. Its generated torque follows

$$T_{mag} = m \times B, \tag{2.3}$$

where m is the magnetic dipole moment and B the local geomagnetic field.

Chapter 3

Background

In this chapter the background necessary to understand the problem addressed in this work shall be presented. Starting with relevant orbital mechanics and propagation methods ICARUS selected orbit is also addressed addressed. Finally the theoretical foundations of spacecraft attitude dynamics and control are discussed.

3.1 Orbital Dynamics and Mission Orbit

As mentioned before orbit is a very relevant topic for the work to be discussed. In conjunction with its part in the systems controllability the orbit also affects maximum torque produced and external torques affecting the system as altitude affects both points. A simulation of this orbit is therefor necessary for the evaluation of the system being developed. As such, before detailing ICARUS' preferred orbit a brief background on orbital mechanics shall be addressed.

3.1.1 Fundamentals of Orbital Mechanics

With orbital mechanics one can explain how objects move through space. This motion is usually derived from Newton and Kepler laws. A satellite orbiting Earth can be simplified from a two body problem to a central-force problem. As the planets mass is much greater than the satellites, only the satellites motion is affected. This force can be determined using Newton's law of universal gravitation3.1.

$$F = G\frac{m_1 m_2}{r^2} \tag{3.1}$$

Thus it can be deduced [10] that the acceleration caused by earth's gravity is

$$a_{grav} = -\frac{\mu_{earth}}{r^3}\mathbf{r} \tag{3.2}$$

With $\mathbf{r}$ being the satellites position and r its norm. The standard gravitational parameter $\mu = G(m_1 + m_2)$ which in case of an artificial satellite orbiting Earth can be fixed to $3.986004418 \times 10^{14}$ due to the difference in masses of both objects in question.

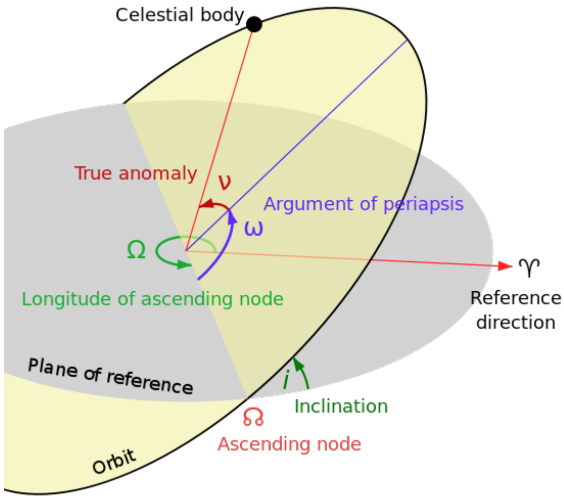

Figure 3.1: Orbital Parameters[11]

To define a Kepler orbit in a two body problem a brief description on the parameters used will be given. Using this parameters the velocity and position of the orbiting object can be calculated. For a more in dept understanding of these mechanics refer to [10]. Figure 3.1 is a visual reference to better comprehend the following parameters used to define orbits

- a: The **semi-major axis** is the distance from the center of mass of the Earth to the orbit apogee.
- e: **Eccentricity** is the value that determines how much the orbit deviates from a perfect circle. This value goes from 0 to 1 for elliptic orbits. For $e \geq 1$ the object follows an escape orbit with either an parabolic or hyperbolic trajectory to infinity.
- i: **Inclination** is the dihedral angle between the orbital plane and the equatorial plane.
- Ω: **Right Ascension of the Ascending Node (RAAN)** is the angle between the reference and the direction of the ascending node, the point where the orbit passes above the equatorial plane.
- ω: **argument of perigee** is the angle between the ascending node and perigee measured in the orbital plane along the direction of motion.
- θ_0: **True anomaly** is the angle between the perigee and the satellites current position.
- **T**: The **period** is not required to define an orbit but will be a used parameter in the following work. The period relates to a and the standard gravitational parameter in the following way

$$\mathbf{T} = 2\pi\sqrt{\frac{a^3}{\mu}} \tag{3.3}$$

- n: The **mean motion** is the average angular velocity of an object in orbit. As for an orbit to be completed a rotation of 2π is required n is defined as

$$n = \frac{2\pi}{\mathbf{T}} \tag{3.4}$$

3.1.2 ICARUS Orbit Selection and Parameters

ICARUS' selected orbit was a Sun-Synchronous Orbit (SSO), a type of polar orbit that maximizes sun exposure time achieving almost no eclipse time during the satellites lifetime. It achieves this by arranging its orbital plane so that, for each revolution of Earth around the Sun, the longitude of the ascending node precesses through one complete revolution around Earth. ICARUS' team reached a range of feasible options for its orbit and is presented in the table 3.1

Table 3.1: Orbit parameters.

Orbital Parameters	Ranges
$a\,(km)$	6828.1-6843.1
$e\,(^\circ)$	0.0001 ± 0.0001
$i\,(^\circ)$	97.21 - 97.26
$\Omega\,(^\circ)$	190.88 - 11.36
$\omega\,(^\circ)$	0 - 360
$\theta_0\,(^\circ)$	0 - 360
$\mathbf{T}\,(min)$	93.89 - 93.58

This type of orbit does not have its plane concurrent with the geomagnetic equatorial plane. Its affects on the local magnetic field and atmospheric drag will be taken into account when performing simulations.

3.1.3 Orbit Propagation and Simulation Methods

Several approaches exist for orbit propagation, differing mainly in their fidelity and computational complexity. The simplest methods are based on the two-body problem, where the spacecraft is assumed to be influenced solely by Earth's gravitational attraction. In this case, the equations of motion are given by 3.1 and can be integrated numerically using standard methods such as Runge–Kutta schemes. While computationally efficient, this approach neglects perturbations arising from Earth's oblateness, atmospheric drag, solar radiation pressure, and third-body gravitational effects. Higher-fidelity propagators incorporate some or all of these perturbations. Numerical propagators can achieve very high accuracy by directly integrating the perturbed equations of motion, but their computational requirements increase considerably. For CubeSat mission analysis, where simulations often require thousands of Monte Carlo iterations, a balance between accuracy and computational cost is desirable.

A widely adopted solution for Earth-orbiting satellites is the Simplified General Perturbations 4 (SGP4) algorithm [12]. Developed by the North American Aerospace Defense Command (NORAD), SGP4 is the standard propagator used with Two-Line Elements (TLE) sets and remains the most common method for predicting the trajectories of satellites in LEO. Rather than numerically integrating all perturbation forces at every step, SGP4 employs analytical and semi-analytical models to account for the dominant orbital perturbations, including Earth's oblateness, secular and periodic gravitational effects, and atmospheric drag. Its low computational footprint makes it particularly suitable for CubeSat mission analysis, ensuring reliable position estimation with errors typically ranging from a few hundred meters to several kilometers.[13]

3.2 Attitude Dynamics and Control Modeling

3.2.1 Reference Frames for Spacecraft Attitude Representation

To control the spacecrafts orientation, knowledge on the reference frames used in space applications is necessary. For this purpose the following sections shall describe the most common reference frames used.

3.2.1.1 Spacecraft Body Frame

The Spacecraft Body Frame, mostly used for assembly purposes, for attitude control will serve as the navigational base to be controlled in relation to an external reference frame. ICARUS body reference frame has its axis perpendicular to its faces as demonstrated in figure 3.2 and its center in the satellite center of mass.

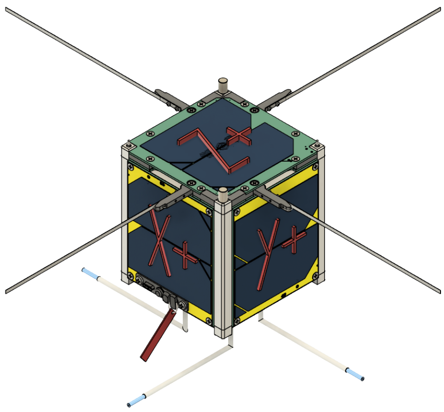

Figure 3.2: Spacecraft Body Frame

3.2.1.2 Inertial Reference Frames

An inertial coordinate system has no acceleration relative to an object not affected by any measurable forces, thus is one in which Newton's law's of motion may be applied. A frame with constant velocity and without rotation in relation to an inertial frame is also classified as inertial. Celestial Reference frames have their axes fixed to distant stars in order to achieve the best approximation of an inertial frame. The International Celestial Reference Frame (ICRF) and has its axes fixed with respect to the positions of several very distant extragalactic sources. The z axis is aligned with Earth's magnetic North, and the x axis with the vernal equinox. Its origin is located at the solar system center of mass.

3.2.1.3 Geocentric Frames

As the satellite in discussion is Earth orbiting, a frame of reference with its origin in Earth's center of mass is more appropriate. Within this spectrum there are two options:

- Geocentric Inertial Frame (GCI) has its axis aligned with those of the ICRF, and although it is only an approximate inertial frame due to the linear acceleration of Earth's orbit around the Sun it may still be used in the context of attitude analysis. An example of such a frame is the Earth Centred Inertial (ECI) as shown in the figure 3.3.
- Earth Centred/Earth Fixed (ECEF) is a frame that accompanies Earth's rotation with its x axis pointed to the prime meridian.

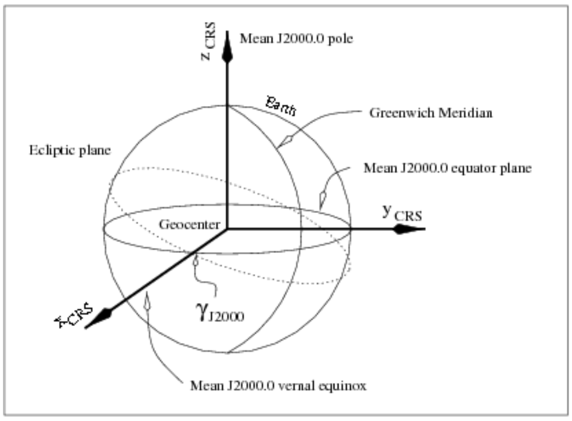

Figure 3.3: ECI[14]

3.2.1.4 Orbit Reference Frame

The origin of this reference frame is situated in the satellites center of mass. Its z axis pointed towards Earth's center of mass and x axis aligned with the satellites velocity makes this frame quite useful for determining motion in regards to Earth. The X_0, Y_0, Z_0 frame in figure 3.4 is a visual representation of this frame.

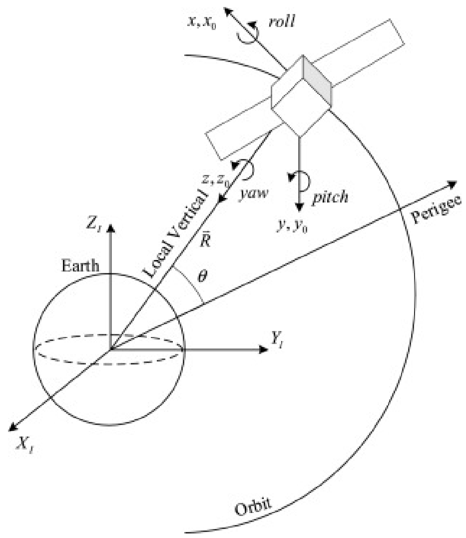

Figure 3.4: Orbital reference frame[15]

3.2.2 Attitude Representation and State Space Formulation

Let us define a state space that represents a satellites attitude and how it changes through time. For representing attitude a rotation matrix in $\mathbb{R}^3$ known as Attitude Matrix (A) or Euler angles are viable options. For efficiency sake, a quaternion representation will be opted for with q being defined by

$$q = \begin{bmatrix} q_1 \\ q_2 \\ q_3 \\ q_4 \end{bmatrix} \tag{3.5}$$

And obeying the relations, as defined by W.R.Hamilton in 1844, $q = q_4 + iq_1 + jq_2 + kq_3$ with $i^2 = j^2 = k^2 = -1$.

As explained in [16] $q(t+\Delta t)$ can be approximated to $q(t) + \frac{1}{2}\Delta\theta \otimes q(t)$ with $\Delta\theta$ being the rotation at Δt . With this it can be determined that

$$\dot{q}(t) = \frac{1}{2}\omega(t) \otimes q(t) \tag{3.6}$$

with $\omega(t)$ being the angular velocities at instant t. As the purpose will be to achieve a commanded quaternion q_c a error quaternion will be used in the state space defined by

$$\delta q = q \otimes q_c^{-1} \tag{3.7}$$

The angular velocity dynamics follow

$$\dot{\omega} = -J^{-1}([\omega\times]J\omega + L), \tag{3.8}$$

$$[\omega\times] = \begin{bmatrix} 0 & -w_3 & w_2 \\ w_3 & 0 & -w_2 \\ -w_2 & w_1 & 0 \end{bmatrix}$$

Mission requires orientating the satellite to the direction of its velocity vector. This vector, represented as q_c, is not constant as such δq depends on $\delta\omega(t) = \omega(t) - \omega_c(t)$. With ω_c being q_c angular velocity. ω_c's value is not constant through time but can be approximated to as its variation is very small. With a practically circular orbit, seen in ICARUS' desired orbit eccentricity 3.1, it is evident that

$$|\omega_c| = \frac{2\pi}{T} \tag{3.9}$$

Albeit orbital period is not constant its rate of change is very small during its lifetime of 5 years. Thus the assumption of a constant ω_c should not cause significant errors in practice. Consequently $\delta\dot{\omega} = \dot{\omega}$ simplifying the problem and thus equation 3.6 becomes

$$\delta\dot{q} = \frac{1}{2}\delta\omega \otimes \delta q \tag{3.10}$$

In equation 3.8 L represents all exterior torques applied. The most predominant torque will be the control torque produced by the magnetorquer coils, which is defined by equation 2.3.

3.2.2.1 External Torques

External torques refer to all momentum changes produced by the interaction with external entities to the satellite. In space the satellite can be subjected to four types of external torques: gravity gradient torque, magnetic torque, aerodynamic torque, solar radiation pressure torque.

The gravity gradient torque occurs due to the gravitational field of unsymmetrical bodies. The actual gravity gradient depends on the nonspherical gravity field nonetheless, for this types of applications it is usually adequate to approximate to spherical. Thus the gravity gradient torque being used will only depend on the on the non-symmetry of ICARUS' body. Hence this torque will be defined as defined in [17]

$$T_{gg} = \frac{3\mu}{\|r_{gc}\|^3} c \times (Jc) \quad , \quad c = A\frac{r_{gc}}{\|r_{gc}\|} \tag{3.11}$$

with r_{gc} being the position vector of the satellite in its orbit and A the attitude matrix.

Despite most magnetic torque the satellite should be subjected to is caused by the on board magnetorquers, these components are not the only source. This type of torque also occurs due the satellites electronics, parasitic currents or magnetized ferromagnetic materials. Thus this type of torque can't be analytically determined and shall be measured at a more advanced phase of the project, until such measurements are made it shall be assumed 0 for simulation purposes, but all algorithms shall be designed without this assumption.

Although usually atmospheric drag is not of concern when concerning satellites at low enough altitudes it is still relevant. In ICARUS' case this force will be the main factor of it finite lifetime as such aerodynamic torque can not be disregarded. To calculate the cross-product between the aerodynamic drag force($\mathbf{f}_d^b$) and the relative position of the center of aerodynamic pressure and the center of mass($\mathbf{r}_c$).

$$T_a = \mathbf{r}_c \times \mathbf{f}_a \quad , \quad \mathbf{f}_a = -\frac{1}{2} C_d S \rho \|\mathbf{v}\| \mathbf{v} \tag{3.12}$$

With S being the area affected by aerodynamic drag, $\mathbf{v}$ the satellites velocity vector and C_d the drag coefficient which is usually ~ 2 for flat plates[17]. Determining atmospheric density ρ is a much more complex matter and for that the aid of public available model such as NRLMSISE-00 Atmospheric model or similar shall be used.

Although solar radiation pressure torque can be calculated similarly to the aerodynamic torque, at low altitudes this the radiation pressure force ($\mathbf{f}_s$) is dominated by aerodynamics as its value is extremely low. Nevertheless it can be estimated if the need arises with the aid of solar pressure models. For a better understanding of how to simulate this effects [17] offers a good explanation.

With this the state x can be defined with the following state space

$$\dot{x}(t) = f_n(x) + b_n u_n + d_n(x,t) \tag{3.13}$$

$$f_n(x) = \begin{bmatrix} \frac{1}{2}\left([\delta q \times]\delta\omega + \delta q \delta\omega\right) \\ -\frac{1}{2}\delta q \delta\omega \\ -J^{-1}\left([\delta\omega\times]J\delta\omega\right) \end{bmatrix} \tag{3.14}$$

$$b_n = \begin{bmatrix} 0_{3\times3} \\ 0_{1\times3} \\ -J^{-1} \end{bmatrix} \quad , \quad u_n = (NAI) \times B \tag{3.15}$$

$$d_n(x,t) = \begin{bmatrix} 0_{3\times1} \\ 0 \\ -J^{-1}\left(T_{gg}(x,t) + T_m(x,t) + T_a(x,t)\right) \end{bmatrix} \tag{3.16}$$

Chapter 4

Magnetic Attitude Control Methods

In this Chapter it shall be reviewed the state of the art in magnetic attitude control. Starting with an overview of strategies used followed by a deeper analysis on those more suitable for small satellites. In this thesis a sliding mode approach will be analyzed and compared to PD control law. These options where chosen has they are the most appropriate for the 1U cubesat platform in question. More complex approaches where pondered but ultimately excluded due to the low computing power of the MCU(2.1.2) used. As such the following analysis will in dept for these methods

4.1 Overview of Magnetic Attitude Control Techniques

Magnetic attitude control has existed in satellites since the beginning of the space exploration. During the early decades of the space era permanent magnets where very popular to give a rough attitude stabilization around the local geomagnetic vector. Hysteresis rods such as the one used in Sweden's Munin nano-satellite[18] offered and angular velocity damping. The first active magnetic actuators for attitude control where flown in Tiros II[19] in 1960. Since then active magnetic control has evolved tremendously, with fully magnetically controlled satellites orbiting Earth currently. In the following paragraphs a list of active magnetic control methods used today shall be presented.

Magnetorquers do not produce significant torques, mainly due to the low values of the intensity of the geomagnetic field, so the most common use for active magnetic actuator is for momentum dumping[16] [20]. This is not much of attitude control as it is more of a support for other attitude actuators, mainly reaction wheels.

The most common use for magnetorquers following this is in angular velocity damping or detumble. Even satellites that don't have requirements concerning pointing usually still need some form of detumble. During deployment procedure it is not unusual to have satellites placed in their preferred orbit with high values of angular velocity, this can hinder basic mission procedures including ground communications. The most common used algorithm used in this situation is the B-dot algorithm[16], [21], [22]. In 2020 Nicolas Petit and Ioannis Sarras propose a generalized control law that is Uniformly, Globally Exponentially Stabilizing (UGES) and show that the B-dot control law is a particular case of the law[23].

Classical feedback laws[24][25] and sliding modes[26][27] are commonly employed in satellites of these dimensions. These solutions are simple and computationally effective which make them very popular among cubesat developers. More complex solutions using Model Predictive Control (MPC)[28][29] or linear optimizations[30][31] have also been proposed but such methods require computational power that is not usually available in satellites as small as cubesats. Although data-driven and neural-network-based control techniques have recently been explored [32], their application to spacecraft attitude control remains at an early stage.

4.2 Classical Control Approaches for Magnetorquer Systems

4.2.1 B-dot Detumbling Algorithm

When any satellite is launched into space it is very common that the detachment procedure induces some angular velocity into to the spacecraft. This can be detrimental to early satellite operations. Spacecraft antennas might require low angular velocities to ensure proper communication link, or maybe solar panels arrays or other deployable mechanisms might not be able to handle those initial conditions. Lowering this initial angular velocity to an acceptable level is usually the first maneuver performed by any satellite, this is called the detumble phase.

The B-dot algorithm is the most common algorithm used in small satellites for this purpose. The reason for its wide spread use is its simplicity and robustness to attitude uncertainty.

This algorithm follows the following law:

$$m = -\frac{k}{\|B\|}\omega \times b \tag{4.1}$$

where m is the produced magnetic dipole,ω is the angular velocity, B is the magnetic field sensed by the onboard magnetometers, $b = B/\|B\|$ and k a control variable[16]. The control variable u can then be determined using the magnetic torque formula in 2.3.

As this solution is only a particular case of the one purposed in [23] it is only capable of reducing angular velocity to a value in the same magnitude as orbit rate a more than sufficient value for ICARUS' needs in this phase.

k can be a constant positive value but [33] provides the following gain expression

$$k = \frac{4\pi}{\mathbf{T}}(1 + \sin\zeta_m)J_{min} \tag{4.2}$$

with ζ_m being the inclination of the spacecraft orbit relative to the geomagnetic equatorial plane, $\mathbf{T}$ de orbital period and J_{min} the minimum principal moment of inertia. Simulations for the B-dot algorithm where done using this gain expression multiplied by a factor of 10 to increase system response.

4.2.2 Quaternion Based Proportional Derivative Control

In [24], a quaternion based PD control law is proposed for rigid body attitude stabilization, guaranteeing *local exponential stability* under appropriate gain selection and scaling between the proportional and derivative actions. The control input is given by

$$u = -\left(\varepsilon^2 k_p \mathbf{q} + \varepsilon k_v J \omega\right), \tag{4.3}$$

where $\mathbf{q}$ is the vector part of the attitude quaternion, ω is the angular velocity expressed in the body frame, J is the spacecraft inertia matrix, $k_p > 0$ and $k_v > 0$ are the proportional and derivative gains, respectively, and $\varepsilon > 0$ is a scaling parameter. The parameter ε enables independent tuning of the attitude and rate dynamics and is shown in [24] to be essential for establishing exponential stability.

The stability result holds provided that the gains satisfy

$$k_v^2 > k_p \frac{\sigma_{\min}^2(\Gamma)}{\sigma_{\min}(J)} \sqrt{CN(\Gamma)}, \tag{4.4}$$

where $\sigma_{\min}(\cdot)$ denotes the minimum singular value, $CN(\cdot)$ the condition number, and

$$\Gamma = \lim_{T\to\infty} \frac{1}{T} \int_0^T [b(t)\times][b(t)\times]^T \, dt,$$

with $[b(t)\times]$ denoting the skew-symmetric matrix associated with the geomagnetic field vector $b(t)$ expressed in the body frame. Under this condition, the closed-loop system exhibits locally exponentially stable behavior in a neighborhood of the desired attitude. Due to the double-cover property of unit quaternions, both q_c and $-q_c$ correspond to a stable equilibrium.

Although a saturation-aware modification of the PD control law is discussed in [24], saturation effects were not observed to compromise stability within the operational envelope of ICARUS and are therefore not considered further.

For implementation within the nonlinear error-state model defined with 3.14, 4.7, 3.16 equations, the same control structure as in (4.3) is retained by replacing the absolute attitude and angular velocity with their corresponding error variables, i.e., $\mathbf{q} \mapsto \delta q$ and $\omega \mapsto \delta\omega$. This yields the control law

$$u = -\left(\varepsilon^2 k_p \delta q + \varepsilon k_v J \delta\omega\right). \tag{4.5}$$

This change of coordinates preserves the local structure of the closed-loop system around the equilibrium, and thus the local stability properties established in [24] remain valid in a neighborhood of the desired attitude.

4.3 Sliding Mode Control for Magnetically Actuated Spacecraft

The sliding mode implementation will closely follow the Ahmet Sofyalı paper "Robust and global attitude stabilization of magnetically actuated spacecraft through sliding mode"[26]. The algorithm presented is to stabilize attitude at the origin quaternion $\begin{bmatrix} 0 & 0 & 0 & 1 \end{bmatrix}'$. Thus the adaptation of this algorithm to the ICARUS mission specifics shall be addressed.

In [26] the state space used is slightly different but mathematically equivalent to the one presented in equation 3.15. As $m \times B$ will always have a 0 value component in a reference frame aligned with the local geomagnetic field as any component of m parallel to B shall not produce torque, the following equality can be deduced

$$C_b u = m \times B \tag{4.6}$$

With C_B being the projection matrix to the plane orthogonal to the local geomagnetic field vector B and u being a control vector. With this the equation 3.15 becomes:

$$b_n(x,t) = \begin{bmatrix} 0_{3\times 3} \\ 0_{1\times 3} \\ -J_n^{-1} C_B \end{bmatrix} \tag{4.7}$$

The sliding mode manifold proposed in [26] is defined as

$$s(x,t) = \omega + K_q q + M_{\text{int }q} \int_{t_0}^{t} q \, d\tau + J_n^{-1} \int_{t_0}^{t} [D_B(x,\tau) u] d\tau \tag{4.8}$$

where $M_{\text{int }q} = n K_q K_{\text{int }q}$, n is orbit mean motion(3.4) and $K_q, K_{\text{int }q}$ are control design parameters, and D_B is the projection matrix onto the direction along B Note that only the component $C_B u$ contributes to the control torque, while the $D_B u$ term corresponds to the component along B, which does not generate torque but is included in the manifold design. This is beneficial to the stability of the sliding mode, with $s = \dot{s} = 0$ it can be deduced that

$$\begin{aligned} D_B u &= -J_n \dot{\omega} - J_n K_q (\dot{q} + n K_{\text{int }q} q) \Leftrightarrow \\ C_B D_B u &= 0_{3\times 3} = -C_B [J_n (\dot{\omega} + K_q \dot{q} + M_{\text{int }q} q)] \end{aligned} \tag{4.9}$$

From equation 4.9 it can be concluded that as $s \to 0$ the $J_n(\dot{\omega} + K_q \dot{q} + M_{\text{int }q} q)$ becomes parallel to B. This means that in the plane of continuous control authority (plane orthogonal to B) $J_n \dot{s} \to 0$. This is summarized in the following lemma:

Lemma 1 ([26]) *Under the assumption of no disturbances, i.e., for $d = 0$, the attitude motion of a rigid satellite on such an orbit and on the sliding manifold in (4.8) is uniformly asymptotically stable at the inertial reference state x_n for all values of the sliding surface design parameters k_q and k_{intq}.*

From this manifold the reached control law is

$$u = -\frac{1}{2}J_nK_q(q_4\omega + q\times\omega) + \omega\times J_n\omega - J_nM_{\text{int }q}q - K_{ss}\text{sgn}(s) - K_s s \tag{4.10}$$

Applying the state space in equations 3.14, 4.7, 3.16 to the sliding manifold 4.8 and control law 4.10, the following are reached

$$s(x,t) = \delta\omega + K_q\delta q + M_{\text{int }q}\int_{t_0}^{t}\delta q\, d\tau + J_n^{-1}\int_{t_0}^{t}[D_B(x,\tau)u]d\tau \tag{4.11}$$

$$u = -\frac{1}{2}J_nK_q(\delta q_4\delta\omega + \delta q\times\delta\omega) + \delta\omega\times J_n\delta\omega - J_nM_{\text{int }q}\delta q - K_{ss}\text{sgn}(s) - K_s s \tag{4.12}$$

Proof 1 *Using the sliding manifold condition $s = 0$ and substituting the system dynamics into the Lyapunov candidate proposed in [26], it follows that*

$$\dot{V} = -\delta q^T K_q \delta q < 0,$$

which establishes uniform asymptotic convergence of $(\delta q, \delta\omega)$ to the equilibrium.

In the reaching phase the following theorem is presented in [26]

Theorem 1 ([26]) *Consider the instantaneously underactuated attitude motion of a rigid satellite with uncertain inertia matrix subjected to environmental disturbances, which is stabilized by the magnetic sliding mode controller (4.8), (4.10). Provided that the satellite's orbital plane does not coincide with the geomagnetic equator plane and the conditions of Lemma are satisfied then the considered motion enters the sliding mode in finite time (at $t = t_s$, $t0 < t_s < \infty$) if the following two conditions hold: 1) the design parameter ks of the continuous reaching law is positive, which is true for its all values; 2) the design parameter kss of the discontinuous reaching law satisfies the condition in 4.13 together with $L_1 \geq L_2$.*

$$kss = kss[x, k_q, k_{int\ q}] > \frac{L_1 + \sqrt{3}L_2}{L_1 - L_2} \times \left[\sqrt{3}\left(\|T_{gg}\|_\infty + \|T_{aero}\|_\infty + \|T_{solar}\|_\infty + \|T_{mag}\|_\infty\right)\right] \tag{4.13}$$

Here;

$$L_1 \triangleq (1-\overline{\delta}_{J1})min(J_1,J_2,J_3) \triangleq (1-\overline{\delta}_{J1})J_{min}, \tag{4.14}$$

$$L_2 \triangleq \left[\overline{\delta}_{J1} + \overline{\delta}_{J2}(1+\overline{\delta}_{J1})\right]max(J_1,J_2,J_3) \triangleq (\overline{\delta}_{J1} + \overline{\delta}_{J2} + \overline{\delta}_{J1}\overline{\delta}_{J2})J_{max} \tag{4.15}$$

Thus, there exists a sliding mode in purely magnetically controlled attitude motion. In other words, the finite time stability of the sliding manifold $s = 0$, which is the equilibrium in the reaching mode, is guaranteed by the designed magnetic spacecraft attitude control system in a global and robust manner.

Following the analysis in [26], Lemma 1 and Theorem 1 remain valid under the change to error coordinates, as the transformation preserves the local structure of the closed-loop dynamics around the equilibrium.

Chapter 5

Simulation Framework and Performance Evaluation

The following chapter begins with a description the simulation environment developed to evaluate the proposed control algorithms with details on its modeling assumptions, numerical methods, and validation procedures. Following this is the presentation and discussion of the simulation results for both static and dynamic pointing scenarios.

5.1 Simulation Framework

5.1.1 Overview of the Simulation Architecture

To assess the performance of the proposed control algorithms, a custom simulation environment was developed in MATLAB for the ICARUS mission. The simulator follows a standard spacecraft dynamics pipeline as shown in figure 5.1. Initial attitude conditions can be set manually or at random. Initial orbital position is obtained from simulated TLE data from desired orbit shown previously in 3.1. To simulate the satellites orbit MATLABs Aerospace ToolBox was used to great effect in the simulator. This toolbox offered several already implemented function of use for this simulator. Nevertheless these functions overhead would increase simulations runtime, consequently some work arounds and some personalized versions of existing function were required to diminish simulation runtime. The most relevant in this discussion was orbit simulation and is further discussed in 5.1.2.

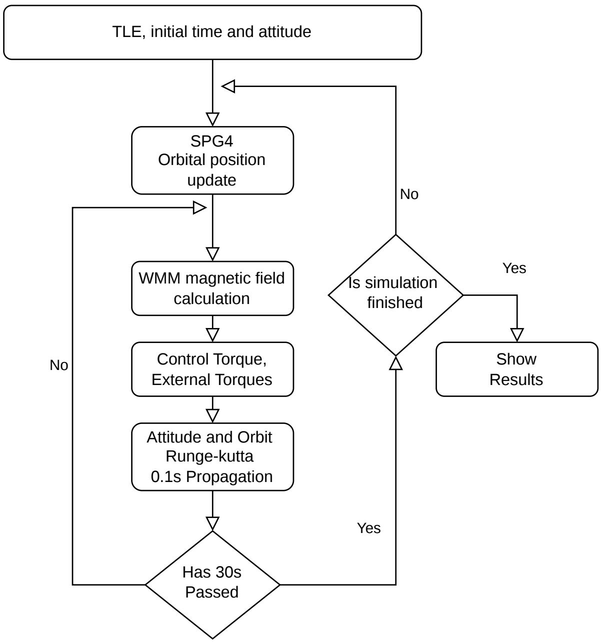

Figure 5.1: Simulator single iteration flowchart

At the end of the simulation data collected is presented in graphs similar to those shown in the following sections. A render of the ICARUS traveling through earth is also shown at this stage to visually confirm that the satellite pointed to the desired position as seen in Fig. 5.2.

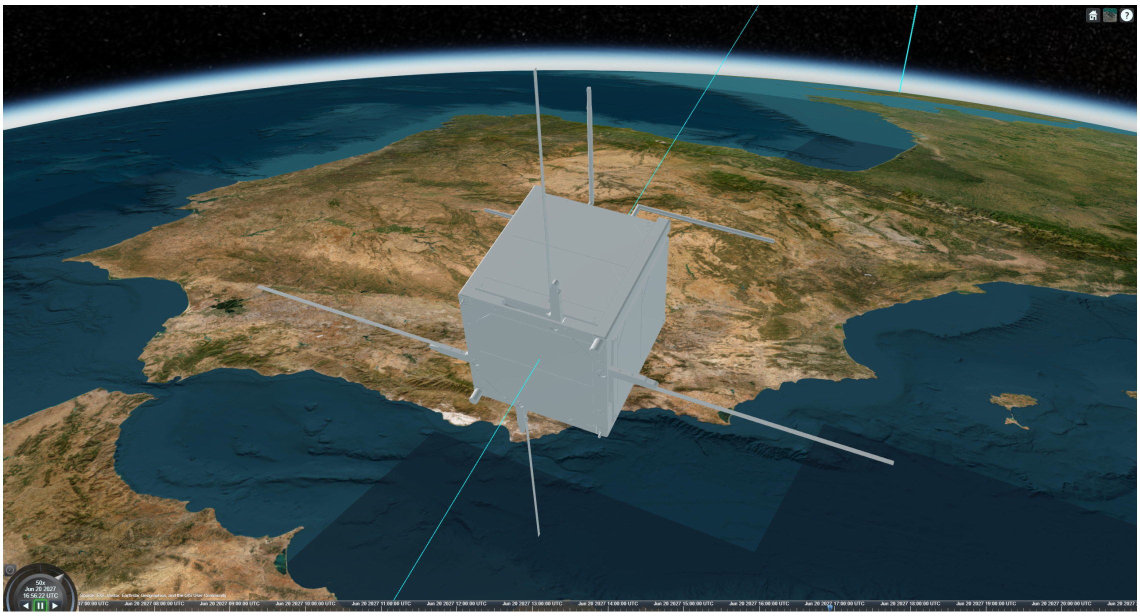

Figure 5.2: Simulator render of ICARUS

5.1.2 Orbital and Environmental Modeling

As mentioned above MATLABs Aerospace ToolBox functions had a lot of overhead that would increase simulation time. To diminish these inefficiencies, orbital position and velocity was mostly done using a Runge-Kutta integration. The previous iteration velocity and equation 3.2 where used to propagate position and velocity respectively. This method doesn't take into account Earth's oblateness,secular and periodic gravitational effects, and other effects that alter the satellites in space. To counter act the errors from the exclusion of these effects, corrections from MATLABs SGP4 each 30 seconds in simulation time is done as shown in figure 5.1. For the altitudes analyzed these two methods didn't diverge in their values in $30s$ achieving error in orbital position and velocity in the order of magnitude of $1m$ and $0.1m/s$ respectively. These errors are negligible once the values expected are in the order of magnitude of $10^6 m$ and $10^3 m/s$ for orbital position and velocity respectively. This method allowed a quicker runtime with periodic corrections for Earths oblateness and effects due to aerodynamic drag without resorting to implementing a SGP4 algorithm from scratch.

With the position and velocity of the satellite determined, gravity-gradient torque and local geomagnetic field are then computed, the latter using the World Magnetic Model (WMM). A personalized version of the toolbox "*wrldmagm*" function with less overhead was used for these computations.

5.1.3 Control Implementation

Thereafter target attitude and angular velocity are determined from the satellites orbit reference frame position and orientation in the ECI frame. The targets then pass through a low-pass filter before control laws are applied. This aids in the convergence of the systems state as shown in Fig 5.3 and 5.4. These figures where done with a single iteration simulation as an example of the effects of this filter.

It is noticeable that, in the example without the low pass filter shown in Fig. 5.3, although the system did converge, at the end of simulation the satellites quaternion (blue) starts diverging from the target (orange). On the other hand, the example with the low pass filter shown in Fig. 5.4 manages to maintain its quaternion (blue) close to the target (orange).

Finally after this filter the control law is applied to determine magnetic torque. The ideal torque from which ever law from the ones show in Chapter 4 is currently being analyzed is calculated. Following this, the ideal torque is converted to the actual torque the satellite can produce given its restrictions. Current passing throw each of the magnetorquer coils is also calculated at this stage using 2.2.

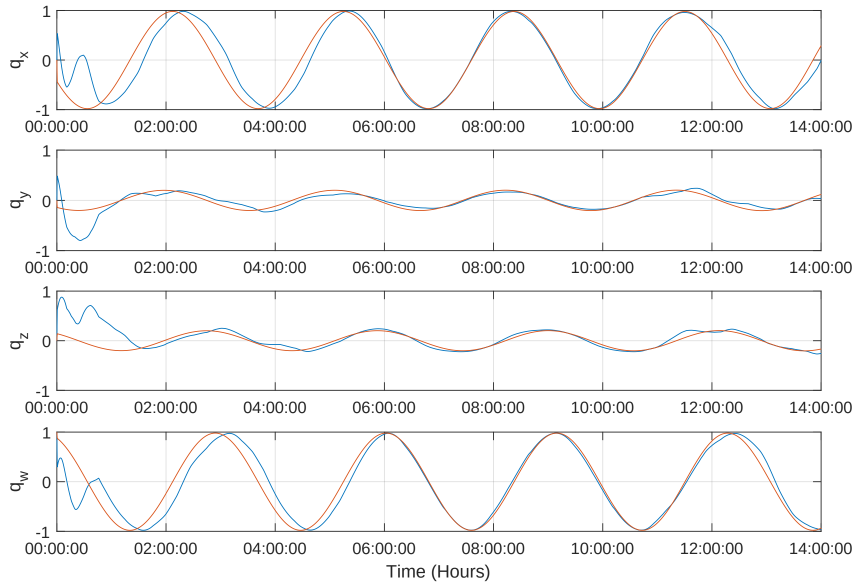

Figure 5.3: Sliding mode quaternion response to dynamic target without low-pass filter: attitude quaternion(blue) and target quaternion (orange)

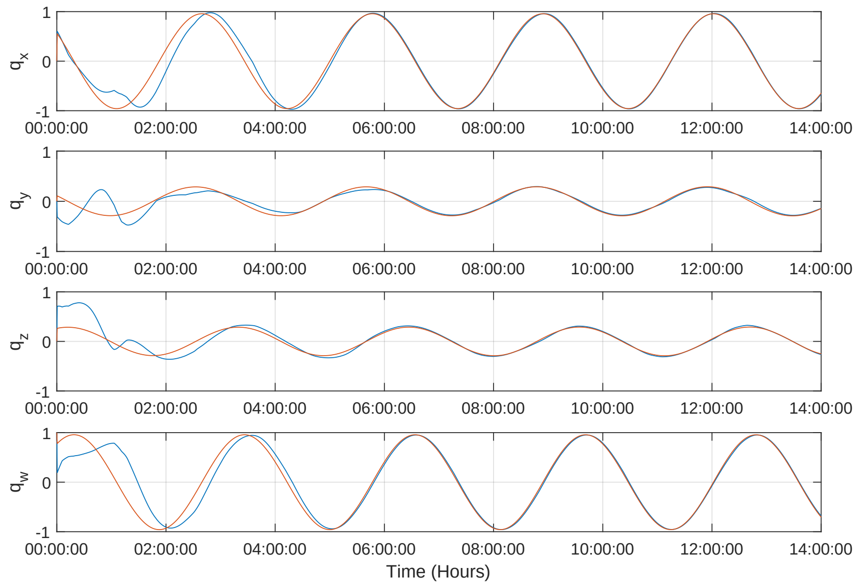

Figure 5.4: Sliding mode quaternion response to dynamic target with low-pass filter: attitude quaternion(blue) and target quaternion (orange)

5.1.4 Spacecraft Dynamics and Numerical Integration

As discussed previously, other environmental disturbances are neglected. This implementation choice can lead to divergence when comparing to a real life scenario, as atmospheric drag is still a factor that should be taken into account in the desired orbit altitude. The implementation of this torque although possible would require more time and computing power to be done effectively. Nevertheless the torques generated from atmospheric drag should be significantly smaller than the one from the satellites magnetorquers. Finally all torques are summed and applied to the attitude dynamics. Which subsequently are propagated using a fourth-order Runge-Kutta integration scheme using the dynamics explained in subsection 3.2.2 in their normal formulation, not the error form used in the control laws.

5.1.5 Simulation Setup and Performance Metrics

Initial conditions are randomized for each Monte Carlo iteration and run in parallel. For pointing simulations a prior detumbling phase is assumed, therefore, the initial angular velocity magnitude is fixed at 0.8°/s. Detumble simulations initial angular velocity magnitude is also fixed but at various different values to ensure proper response for all possible cases. Unless otherwise stated, all reported results correspond to averages over 200 Monte Carlo simulations. Quaternion averaging is performed using the method described in [34], while dispersion is reported in Euler angles to facilitate comparison with the pointing requirement 1. Power consumption is calculated from the current i used to produce the control torque with equation 2.2 and

$$P = i^2 R \tag{5.1}$$

with R being the magnetorquer coil electrical resistance.

5.2 Performance Evaluation

All pointing simulations assume an initial detumble prior. This is to simulate a more accurate state of the satellite when performing a pointing maneuver. As the satellite will always try to maintain some control of its angular velocity even when not performing its scientific duties, as to ensure reliable communication with the ground station.

For an initial detumble and this constant angular velocity control the B-dot algorithm is perfect. So before evaluating the control laws for the pointing purpose, some simulations ensuring that detumble is possible where conducted. Additionally these simulations serve to test the simulator with a simple and widely used method to control attitude using magnetic actuators. Hence validating the simulator for following simulations.

Thereafter pointing analysis starts. Firstly a static target scenario is considered to evaluate controller stability and steady-state accuracy. Following this a dynamic target scenario is considered, corresponding to the mission requirement of maintaining the Langmuir probe aligned with the ram direction.

5.2.1 B-dot Algorithm Detumble Performance

Three detumble simulations where conducted using the simulator, all with 200 iterations of the Monte Carlo setup. Simulations where conducted with initial attitude and angular velocities randomized. Angular velocities had their magnitude fixed at $20°/s$, $240°/s$ and $80°/s$ to simulate a common case, the worst case scenario and an intermediate value for angular velocity post deployment from the launcher.

Figures 5.5, 5.6 and 5.7 are the average angular velocities(blue lines) and its variance(light blue area) for each simulation.

It can be observed that all simulations after 4 hours, in about two full orbits achieved an angular velocity of practically $0°/s$. The $240°/s$ case in fig. 5.7 was the slows to achieve this as it had the most aggressive initial angular velocity. While the $20°/s$ case in fig. 5.5 was the fastest achieving the same metric almost one full orbit earlier.

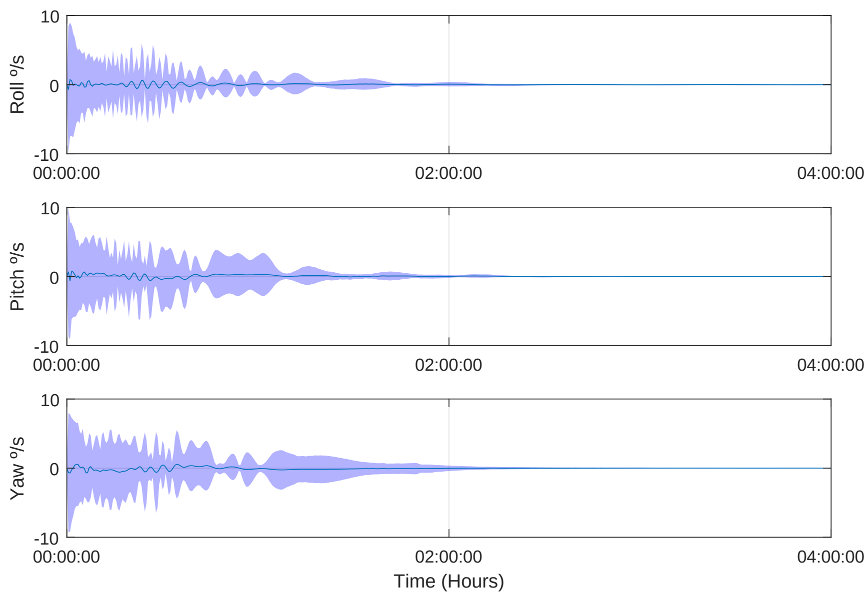

Figure 5.5: B-dot control law: average angular velocity for $20°/s$ initial angular velocity

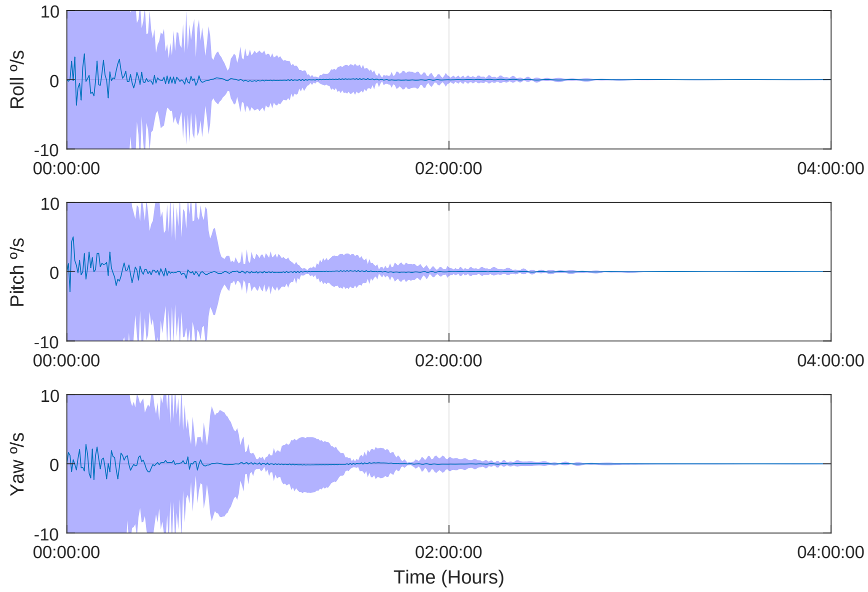

Figure 5.6: B-dot control law: average angular velocity for $80°/s$ initial angular velocity

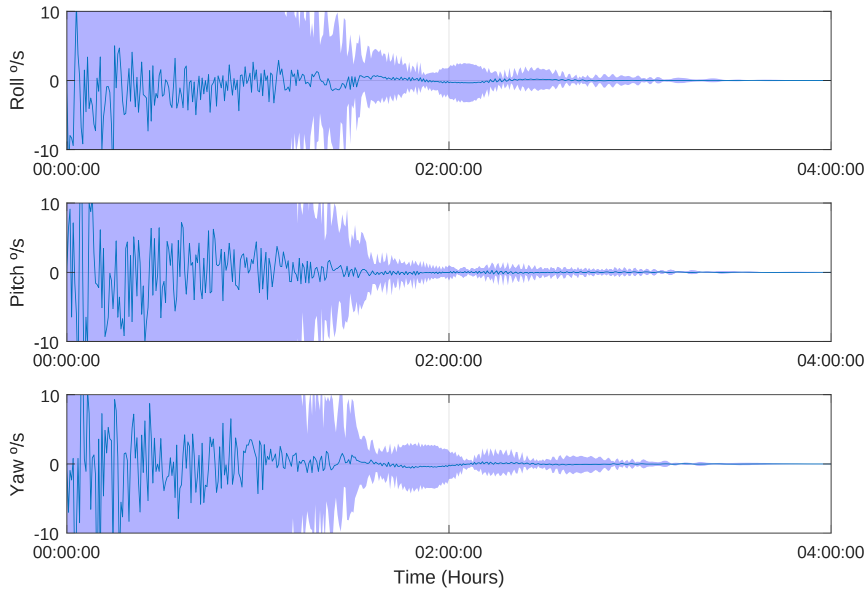

Figure 5.7: B-dot control law: average angular velocity for $240°/s$ initial angular velocity

Table 5.1: B-dot Simulations values at 4 hours

Sim.	**Roll**$^\circ/s$	**Pitch**$^\circ/s$	**Yaw**$^\circ/s$
$20^\circ/s$	$1.327\times10^{-5}\pm1.009\times10^{-3}$	$-1.000\times10^{-4}\pm7.928\times10^{-4}$	$1.452\times10^{-4}\pm9.264\times10^{-4}$
$80^\circ/s$	$6.173\times10^{-5}\pm9.815\times10^{-4}$	$-2.646\times10^{-5}\pm9.244\times10^{-4}$	$-1.408\times10^{-4}\pm1.370\times10^{-3}$
$240^\circ/s$	$-1.113\times10^{-4}\pm1.063\times10^{-3}$	$7.566\times10^{-5}\pm8.452\times10^{-4}$	$-2.139\times10^{-5}\pm9.594\times10^{-4}$

Table 5.1 shows the actual values given by these simulations at their end. With this detumble capability is proven and the simulator is validated. All conditions to evaluate the control laws are gathered.

5.2.2 Static Target Pointing Performance

In the static target scenario the spacecraft is commanded to align with the unit quaternion $\begin{bmatrix}0 & 0 & 0 & 1\end{bmatrix}^T$. As stated above both algorithms run through a Monte Carlo simulation with 200 iterations with different initial attitude conditions of a post detumble satellite. Figures 5.8–5.11 summarize the results for both control laws.

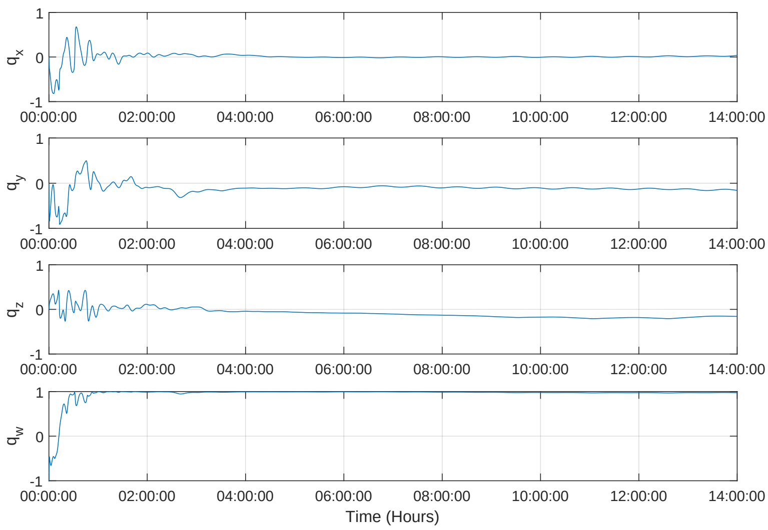

Figure 5.8: PD control law: average attitude error quaternion for a static target

In Fig. 5.8 it can be seen that the PD controller stabilizes at around the 3 hour mark. Although stabilized around the 9 hour mark a slight offset from 0 starts being noticeable for the q_y and q_z parameters of the error quaternion.

On the other hand the sliding mode error quaternion response in Fig. 5.9, seems to stabilize more accurately only showing a small constant oscillation near 0 of the q_y parameter. The sliding mode also shows a slightly faster response, stabilizing around the 2 hour mark.

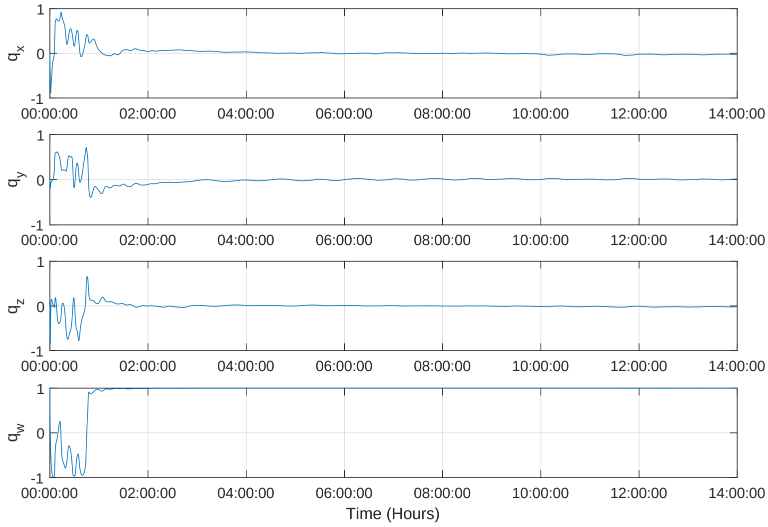

Figure 5.9: Sliding mode control law: average attitude error quaternion for a static target

Figures 5.10 and 5.11 show the simulations average error angle in degrees(dark blue line) and the average variation of the 200 Monte Carlo iterations(light blue area) for the PD and sliding mode control laws respectively.

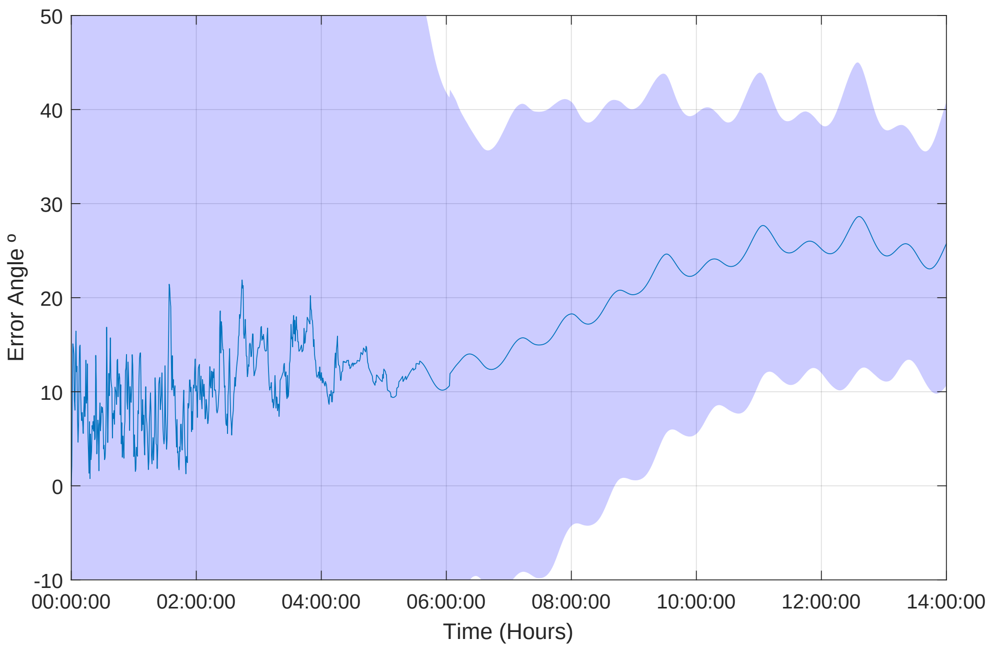

Figure 5.10: PD control law: average Euler-angle attitude error for a static target

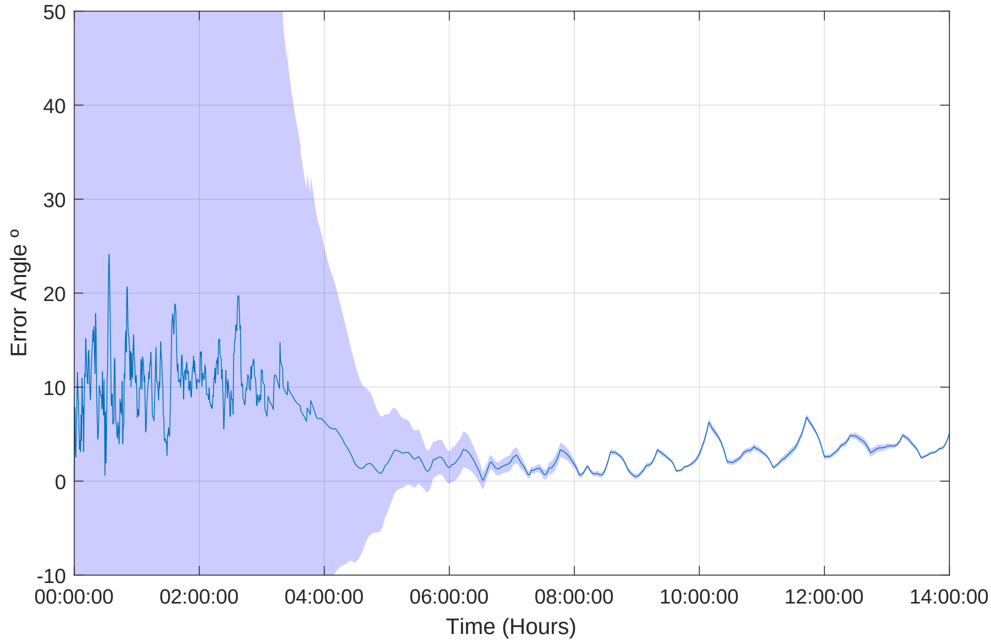

Figure 5.11: Sliding mode control law: average Euler-angle attitude error for a static target

In Fig. 5.10, the PD controller shows a high decrease in variance at around the 8 hour mark to $\pm 20^\circ$ and decreasing until the end of the simulation up to $\pm 10^\circ$. Its average pointing error seems to be better at around $\pm 20^\circ \pm 15^\circ$. Following this at the 10 hour mark when variance has decreased and stability of the system improved average pointing error was shown to increase to approximately 25° oscillating close to this value.

The same response for the sliding mode shown in Fig. 5.11 shows more promising results. The system shows a significantly high decrease in variance at around the 4 hour mark to about $\pm 5^\circ$. It further improves this metric 3 hours after to an almost negligible value. Its average pointing error seems to stabilize early on oscillating around 5°.

Figures 5.12 and 5.13 show the error angular velocities of the satellite in its body frame (blue line) and its variance (light blue area).

In Fig. 5.12, the PD controller seems to achieve a stable response at the 8 hour mark maintaining a small constant oscillation in pitch and roll. Yaw seemingly stabilizes at an saw tooth wave with constant decrease in error followed by an abrupt correction with a bit of an overshoot.

On the other hand, the sliding mode response seen in Fig. 5.13 shows more noticeable and complex oscillations in all axis. Similarly to the other figures of the sliding modes response so far it seems to stabilize around the 4 hour mark.

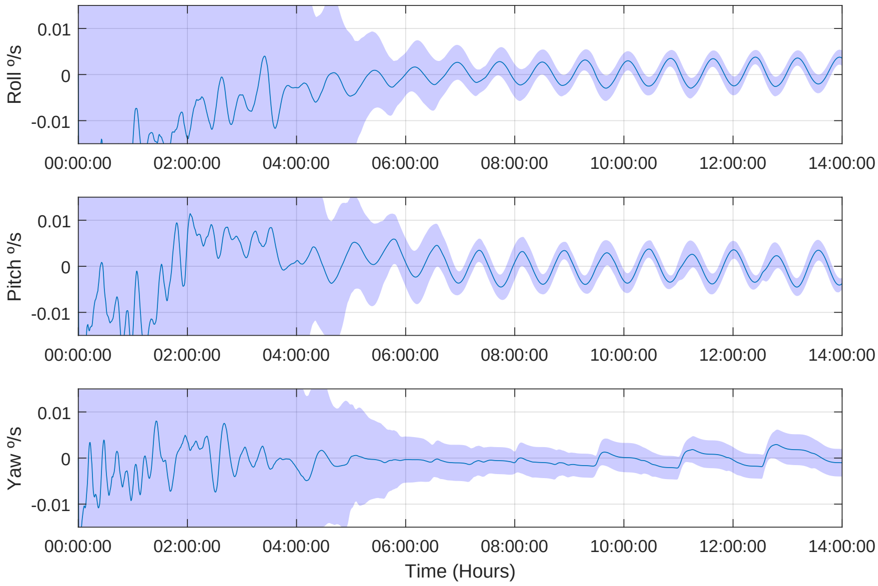

Figure 5.12: PD control law: average error angular velocity for a static target

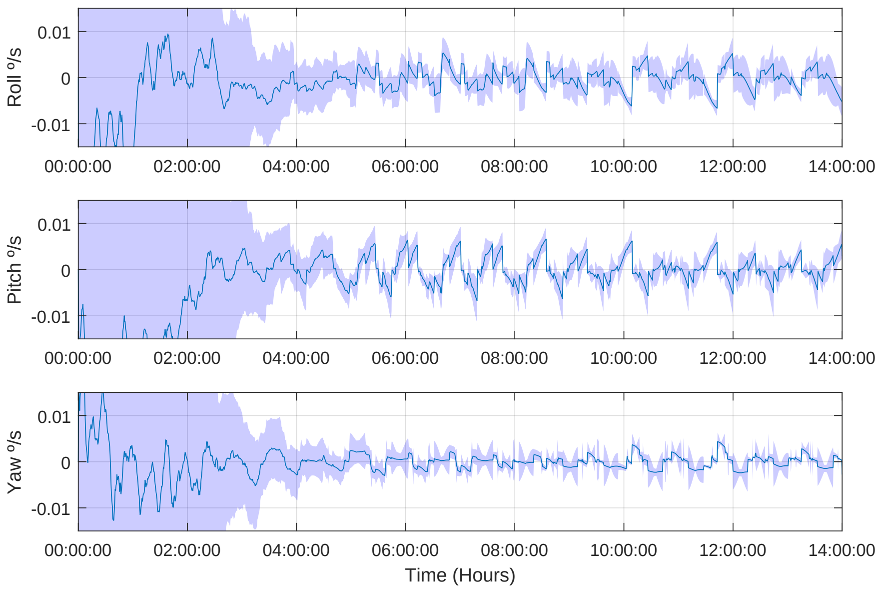

Figure 5.13: Sliding mode control law: average error angular velocity for a static target

5.2.2.1 Discussion of Static Target Pointing Results

These results indicate that, although both controllers stabilize the attitude, the sliding mode law provides markedly superior pointing accuracy. In particular, the sliding mode controller maintains the pointing error within the $\pm 10^{\circ}$ mission requirement, whereas the PD controller exhibits steady-state errors significantly exceeding this bound. All results seem to be consistent in showing that the sliding mode has a faster response stabilizing after 2 to 3 hours after initializing the procedure. Whereas the PD needed 3 times as much time. This might indicate that the PD control parameters where not optimal and could not be using the full capabilities of the system. Nonetheless the results shown in this thesis were the result of the most optimal parameters found for a successful convergence. All attempts of decreasing the response time only resulted the a system divergence.

Residual error observed in both cases as average error angle stabilizes always in an oscillating pattern. This should be the influence of the intrinsic limitation of magnetic actuation. Since disturbances along the geomagnetic field direction cannot be directly compensated, the errors in angular velocities seen in figures 5.12 and 5.13 cause a divergence in the error angle. This can only be compensated once the satellite moves to a point in space where controllability along that angular velocity error is regained. The lower variance in this metric in the sliding mode control law might be a factor of the superiority this law demonstrated in 5.11 even doe both similar average error angular velocities.

Table 5.2 shows the actual values given by these simulations at the 12 hour mark.

Table 5.2: Static case simulation values at 12 hours

Param.	PD	Sliding mode
Quaternion	$\begin{bmatrix} -0.008 & 0.126 & 0.182 & 0.974 \end{bmatrix}$	$\begin{bmatrix} -0.019 & 0.008 & -0.006 & 0.999 \end{bmatrix}$
Error Angle $^{\circ}$	25.179 ± 13.192	2.605 ± 0.228
Error Ang. Vel. Roll $^{\circ}/s$	$-4.212 \times 10^{-5} \pm 3.617 \times 10^{-5}$	$6.023 \times 10^{-5} \pm 1.496 \times 10^{-5}$
Error Ang. Vel. Pitch $^{\circ}/s$	$6.208 \times 10^{-5} \pm 3.407 \times 10^{-5}$	$-9.294 \times 10^{-5} \pm 7.732 \times 10^{-5}$
Error Ang. Vel. Yaw $^{\circ}/s$	$-6.982 \times 10^{-6} \pm 4.868 \times 10^{-5}$	$-3.481 \times 10^{-5} \pm 6.982 \times 10^{-5}$

5.2.3 Dynamic Target Tracking Performance

Figures 5.16, 5.14 and 5.18 show the response of the PD controller. Correspondingly the sliding mode controller response is shown in Figs. 5.17, 5.15 and 5.20.

Both Algorithms show capability to track the dynamic target as seen in Figs. 5.14 and 5.15. In these figures blue lines are average attitude quaternion in the 200 Monte Carlo simulations and orange lines are the target quaternion the system is trying to track.

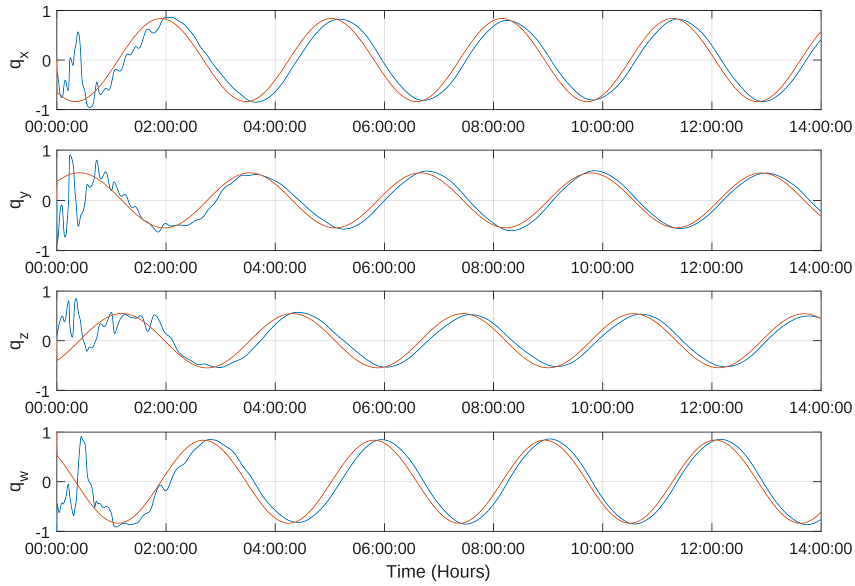

Figure 5.14: PD control law: average attitude quaternion (blue) and dynamic target quaternion (orange)

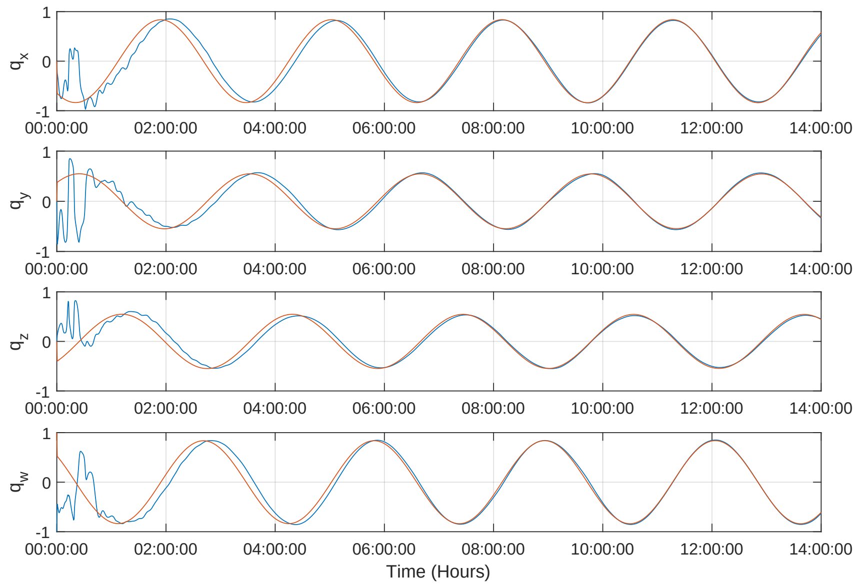

Figure 5.15: Sliding mode control law: average attitude quaternion (blue) and dynamic target quaternion (orange)

In fig. 5.14 the PD controller quaternion follows the target at a slight delay with both never seemingly aligning completely during the duration of the simulation. Its response seems to stabilize in this form since the 4 hour mark, earlier than in its static case response.

The sliding mode in fig. 5.15 on the other hand shows a constant decrease of this delay up until the finish of the simulation. Despite showing at the 4 hour mark a similar delay to the PD control law, by the end of the simulation both attitude and target quaternions overlap.

Figures 5.16 and 5.17 show the error angle through the course of the same simulation. Blue line being the average error angle and the light blue area its variance.

In Fig. 5.16 a significant decrease in variance is first noticed around the 5 hour mark corroborating the observations made in fig. 5.14. Nevertheless thereafter the response seemingly improves up until the 10 hour mark where it stabilizes an error angle around 25° with a variance of ±20°.

The sliding mode in Fig. 5.17 offers a similar response to the PD law with a significant decrease in variance around the 5 hour mark and further improving it until the 10 hour mark. The difference lies in the value to which it stabilizes and the variance achieved, reaching a result of approximately $5^\circ \pm 2^\circ$. This shows that the sliding mode control law despite having a noticeable increase in its variance, still maintains the pointing error within mission requirement throughout the maneuver.

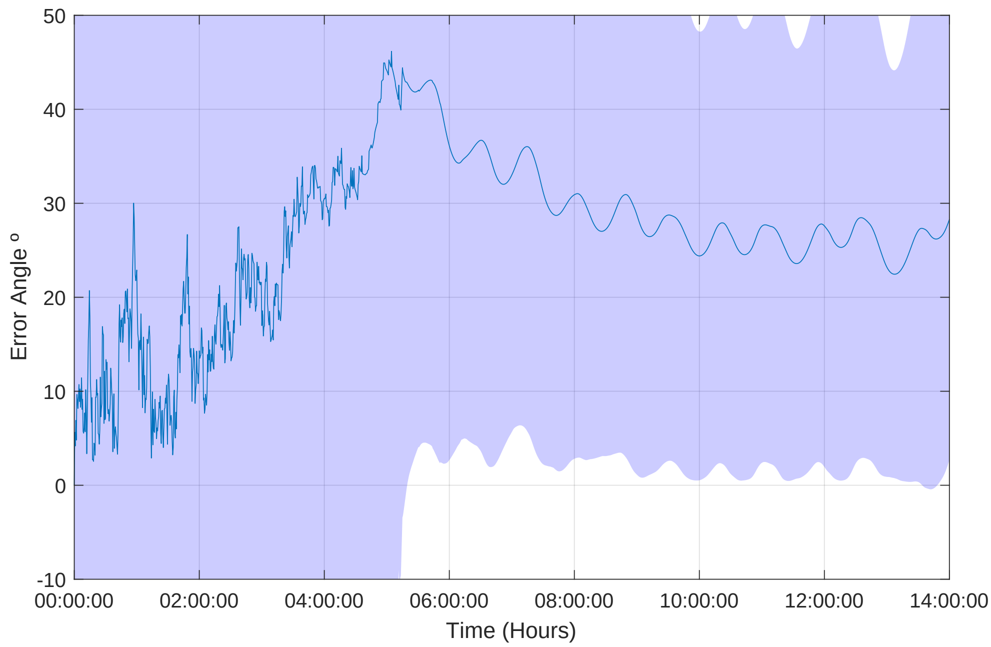

Figure 5.16: PD control law: average Euler-angle attitude error for a dynamic target

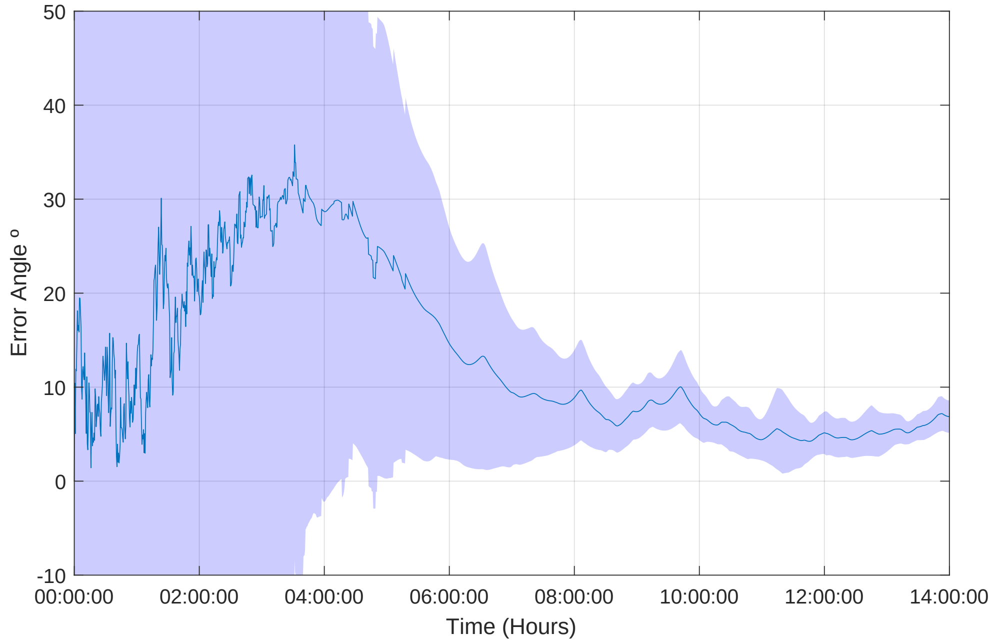

Figure 5.17: Sliding mode control law: average Euler-angle attitude error for a dynamic target

Both responses show a increase in its variance. This behavior can be attributable to its limited ability to regulate nonzero angular velocity under the time-varying and underactuated magnetic control input.

In Figs. 5.18 and 5.20 it can be seen the average angular velocity in blue, and the target angular velocity in orange for both the PD and sliding mode control law respectively. Both values are in the ECI frame. In this frame target angular velocity is constant, this is not the case in the spacecraft body frame. Figures 5.19 and 5.21 show the error angular velocities of the satellite in its body frame (blue line) and its variance (light blue area).

In Fig. 5.18 showcases the difficulty this control law had with non zero angular velocity. The angular velocity stabilizes close to the target but with difficulty remaining there, resulting in an oscillation above or below the target value. Additionally figure 5.19 shows its biggest difficulty was in controlling the satellites pitch and yaw showing a larger dispersion in results.

With Fig. 5.20 the sliding mode demonstrates once more that it is better prepared to handle this scenario. The control law stabilizes with a slight oscillation around the target for roll, pitch and yaw with much smaller variance than the PD controller as seen in fig.. 5.21.

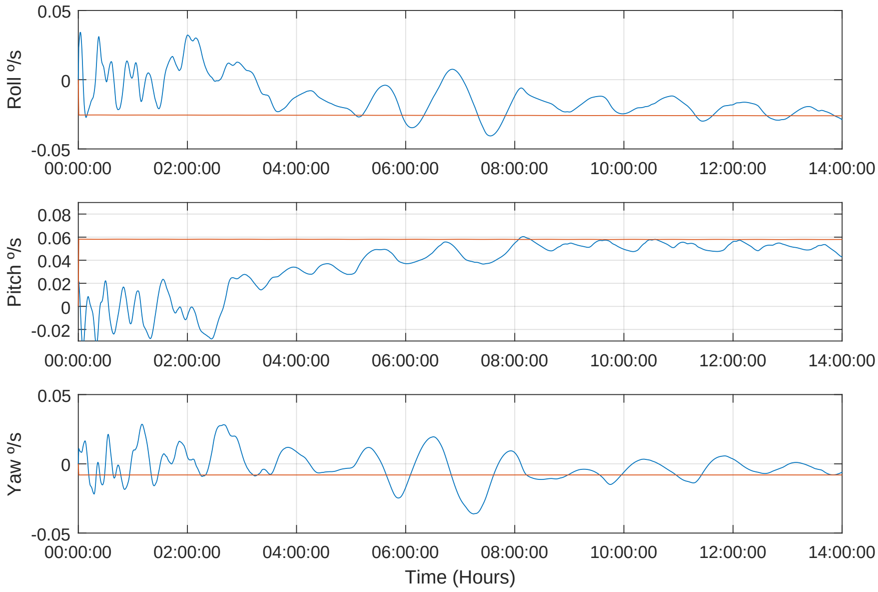

Figure 5.18: PD control law: average angular velocity (blue) and target angular velocity (orange)

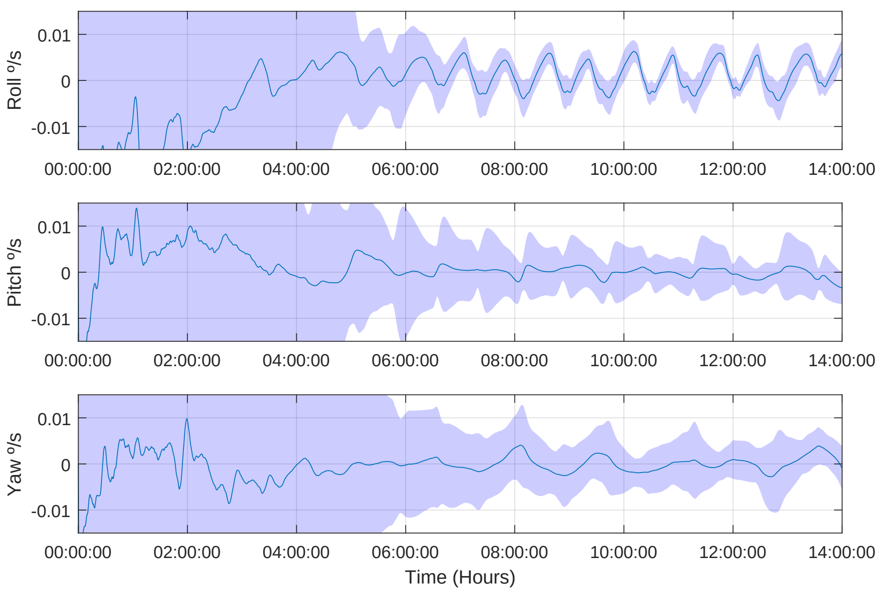

Figure 5.19: PD control law: average error angular velocity for dynamic target

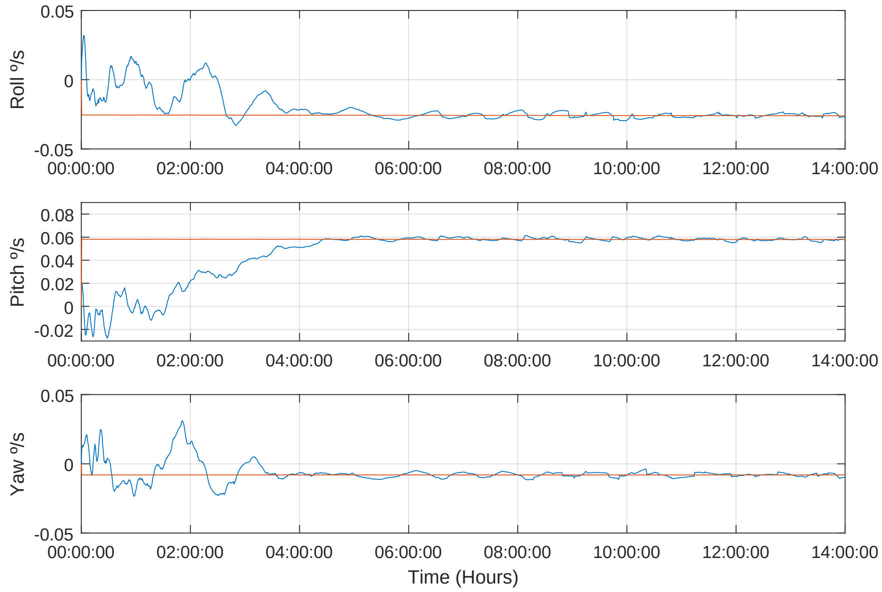

Figure 5.20: Sliding mode control law: average angular velocity (blue) and target angular velocity (orange)

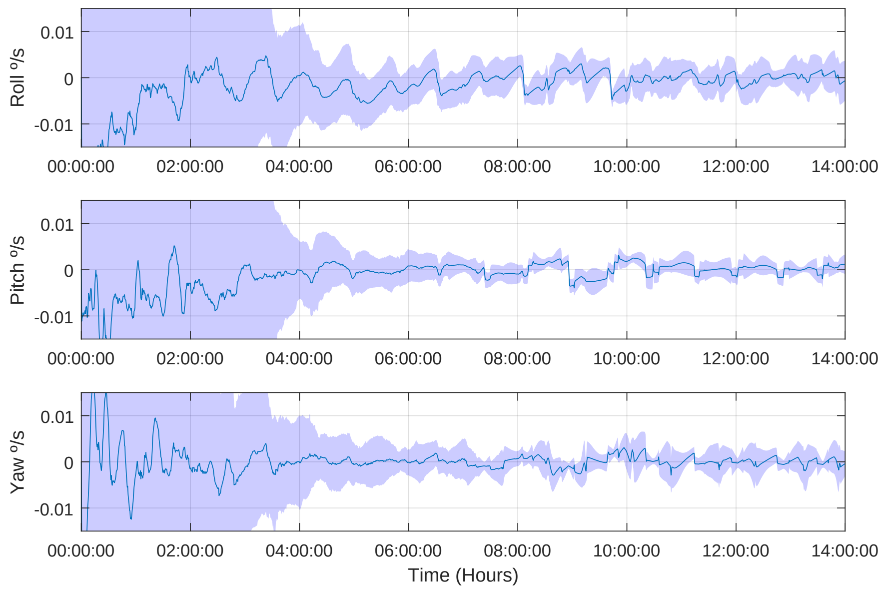

Figure 5.21: Sliding mode control law: average error angular velocity for dynamic target

5.2.3.1 Discussion of Dynamic Target Pointing Results

This dynamic target pointing results clearly show that the PD controller can not compete with the sliding mode in terms of accuracy. Although it can somewhat follow the target, an average error of $25^\circ \pm 20^\circ$ is far from meeting ICARUS 10° requirement. This huge dispersion in results is most likely a result of its response in angular velocity. As stated in 5.2.2.1 due to the intrinsic limitation of magnetic actuation, angular velocity errors result in bigger and harder to control errors in attitude.

The sliding mode control law, on the other hand, showcased an almost identical response in angular velocity in this scenario to its static target analysis. This resulted in an average error of $5^\circ \pm 2^\circ$ meeting ICARUS 10° mission requirement, and proving that the ADCS can perform its duty in allowing the Langmuir probe to conduct its measurements in space.

Table 5.3 shows the actual values given by these simulations at the 12 hour mark.

Table 5.3: Dynamic target case simulation values at 12 hours

Param.	PD	Sliding mode
Error Quaternion	$\begin{bmatrix} 0.233 & 0.030 & 0.028 & 0.971 \end{bmatrix}$	$\begin{bmatrix} 0.035 & 0.012 & 0.024 & 0.998 \end{bmatrix}$
Error Angle $^\circ$	27.593 ± 25.641	5.139 ± 2.260
Error Ang. Vel. Roll $^\circ/s$	$-2.837 \times 10^{-5} \pm 3.525 \times 10^{-5}$	$6.893 \times 10^{-6} \pm 4.053 \times 10^{-5}$
Error Ang. Vel. Pitch $^\circ/s$	$-7.732 \times 10^{-5} \pm 3.937 \times 10^{-5}$	$-2.194 \times 10^{-5} \pm 3.091 \times 10^{-5}$
Error Ang. Vel. Yaw $^\circ/s$	$1.626 \times 10^{-5} \pm 7.276 \times 10^{-5}$	$-3.579 \times 10^{-6} \pm 2.577 \times 10^{-5}$

5.2.4 Power Consumption Analysis

The improved accuracy of the sliding mode controller is accompanied by increased power consumption, a critical constraint for CubeSat missions. An ideal sliding mode tends to have very high control values. To mitigate this effect and reduce power consumption, a saturation function using the ε parameter of value 3×10^{-2} replaced the ideal $\text{sgn}(s)$ term in (4.12) for all these simulations. All sliding mode Monte Carlo results reported used this ε value. To reach this value a trade-off between power consumption and pointing accuracy for the ICARUS system was done.

Figures 5.22, 5.24 and 5.23 show single iteration simulations with equal initial conditions to demonstrate this trade-off. Fig 5.22 demonstrates that lower values ε result in responses close to the ideal $\text{sgn}(s)$.

On the other hand, larger values for this parameter resulted in less power consumed as seen in fig. 5.23. Consequently the systems ability to maintain target attitude reached was reduced even with small increases to this value, as show in fig 5.24. Even higher values where tested but never resulted in the systems convergence.

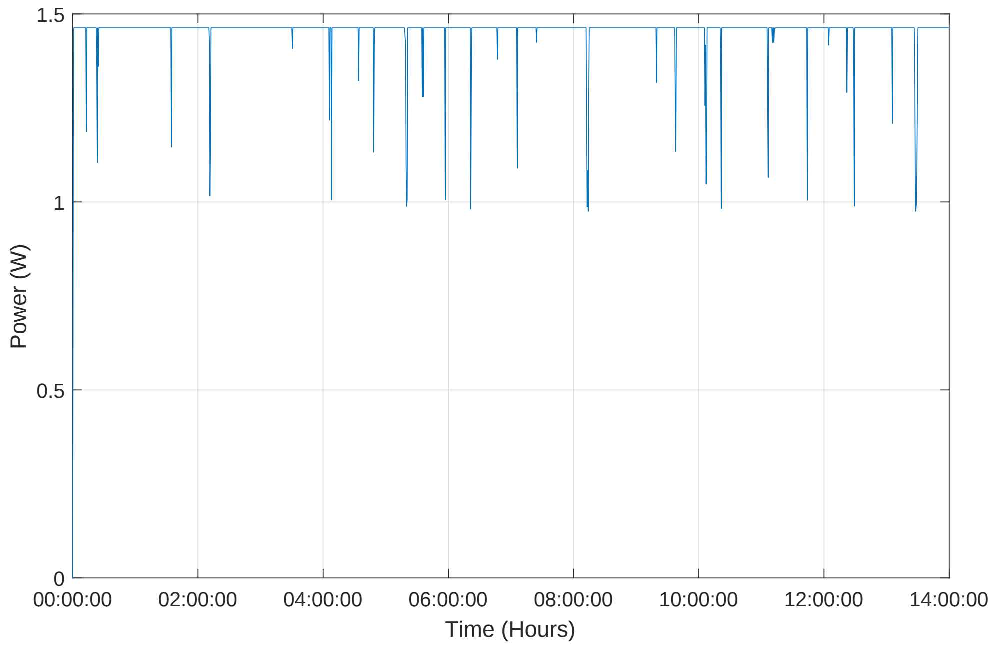

Figure 5.22: Sliding mode control law: power consumption for a dynamic target with $\varepsilon = 3 \times 10^{-3}$

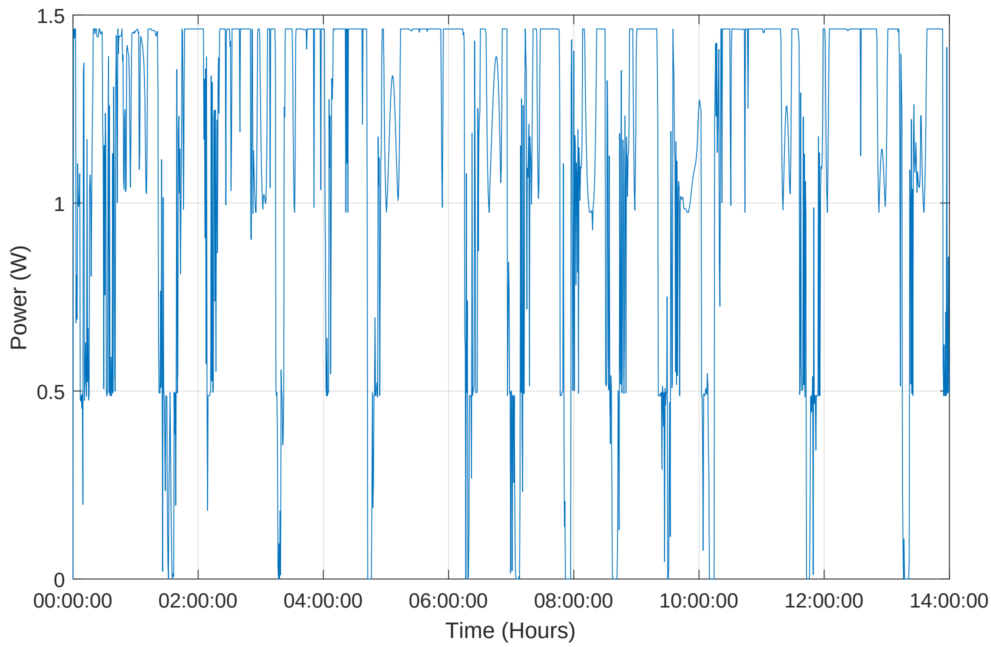

Figure 5.23: Sliding mode control law: power consumption for a dynamic target with $\varepsilon = 3.09 \times 10^{-2}$

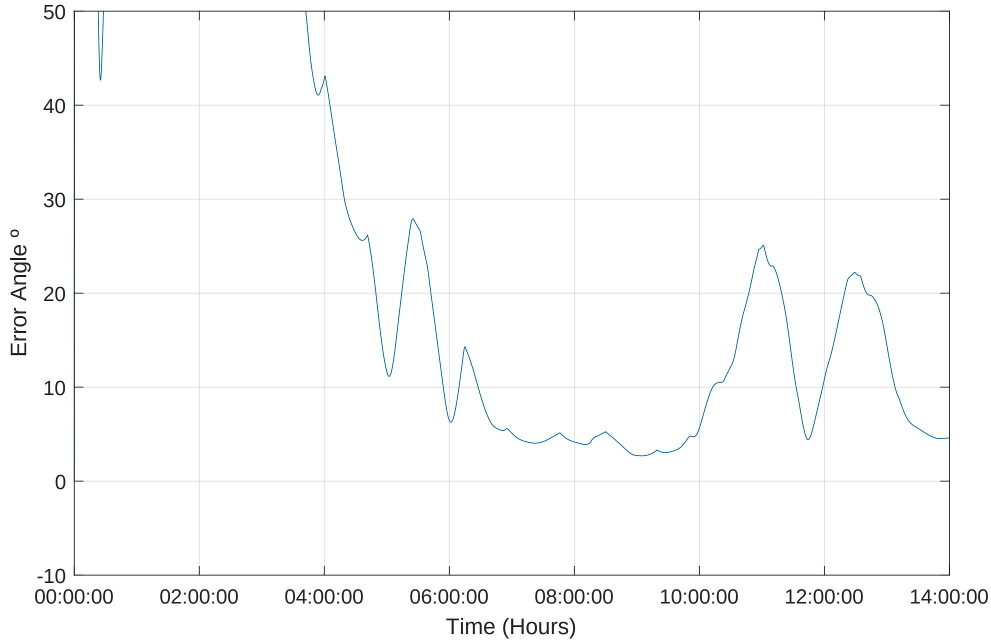

Figure 5.24: Sliding mode control law: Euler-angle attitude error for a dynamic target with $\varepsilon = 3.09 \times 10^{-2}$

Figures 5.25 and 5.26 compare the average magnetorquer power usage over the 200 Monte Carlo simulations for the dynamic target case for the PD and sliding mode control laws, respectively.

Fig. 5.25 shows a very low power usage. With consumption being well below the maximum of $1.5W$ for the ADCS it further confirms the suspicions discussed in 5.2.2.1.

On the other hand, with fig. 5.26 it can be observed that the sliding mode is almost at maximum output for the full duration simulated. This can pose a problem for power management in ICARUS. In the worst case scenario for solar panels power production, this much consumption for this amount of time might not be achievable.

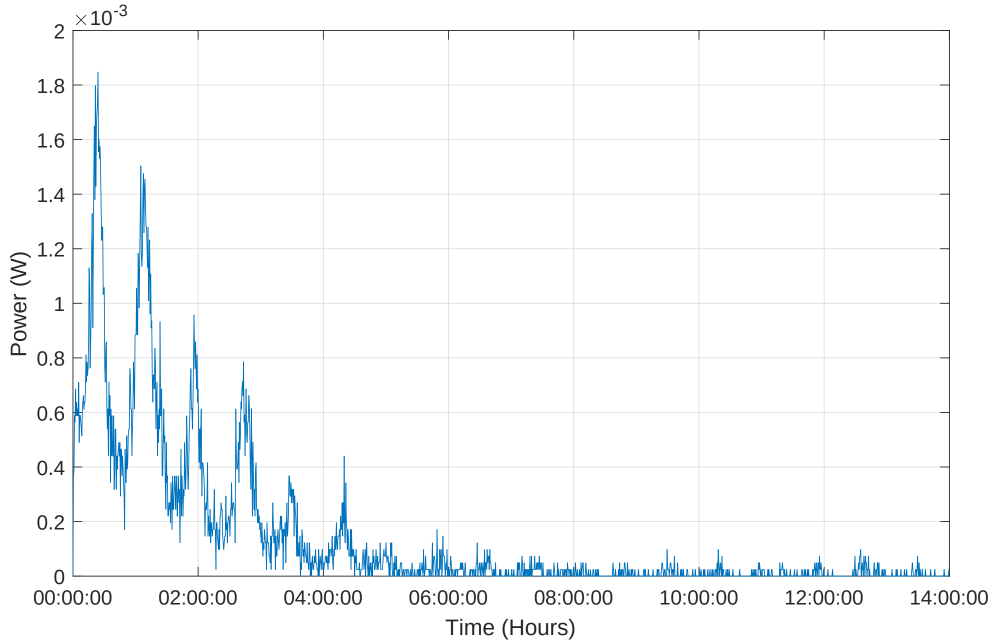

Figure 5.25: PD control law: average power consumption for a dynamic target

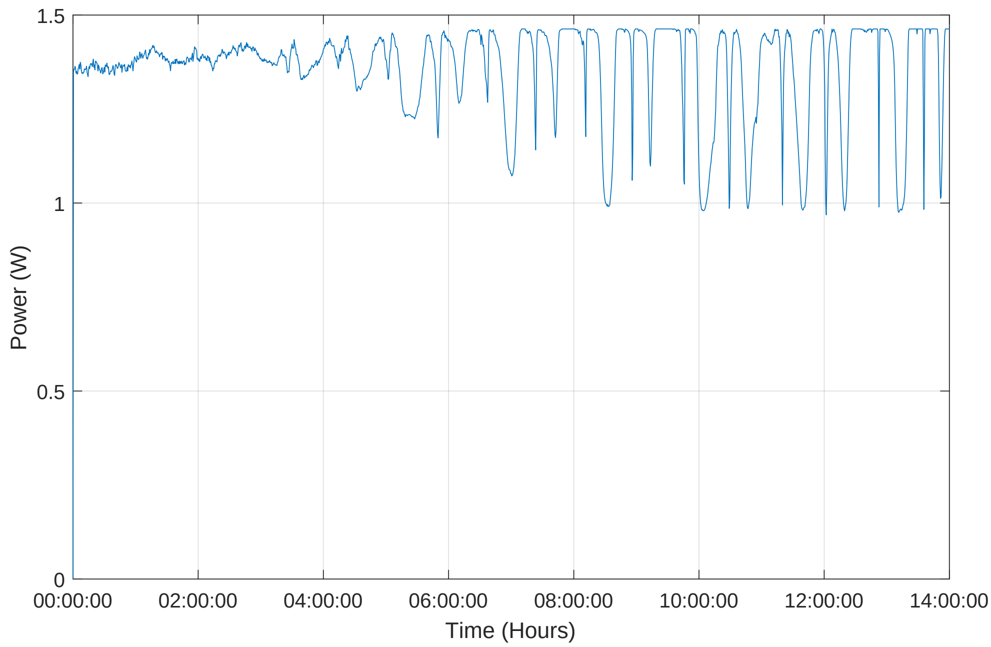

Figure 5.26: Sliding mode control law: average power consumption for a dynamic target

5.2.5 Overall Discussion and Simulation Limitations

In essence, the underactuated magnetic control problem never fully allowed for a stabilization of the attitude. Slight errors in angular velocities would create small divergences in attitude, when aligned with the geomagnetic field. Only compensated once the satellite moved, the geomagnetic field changed and control along that axis was regained. This caused small oscillations around the targets observed in various metrics in both PD and sliding mode for both static and dynamic targets. Despite this the sliding mode managed to outperform the classical PD control law, reaching $5^\circ \pm 2^\circ$ for the scientific mission scenario of a dynamic target while its counter part achieved a $25^\circ \pm 20^\circ$. It is notable that the sliding mode used took into account the effects of external torques such as gravity gradient torque. The PD control law used does not. This is also a factor that benefits the performance of the sliding mode over the more classical approach.

Nonetheless this simulations are not perfect, and further improvements might still be needed. As stated above this simulator still doesn't take into account all external torques. Solar pressure and atmospheric drag will have some contribution to attitude in orbit, although small. Atmospheric drag especially, as ICARUS orbit decays with time, its contribution will increase. With these simulations it is still unclear for how much of the 5 year life time of ICARUS will be able to maintain the capabilities observed in this work.

These simulator so far also assumes the satellite knows its state perfectly. Even doe the determination system was designed to at least be able to determine attitude one degree of magnitude below the reported control capabilities. The determination error will cause an increase in results dispersion.

The power consumed by the sliding mode can also be a problem. These simulations do not take into account battery state. Maneuvers this long might not be feasible in certain conditions. Worst case scenario for power production estimates a third of orbital period in eclipse, this means scientific mission probably is not possible in this conditions. On the other hand this can be resolved by a better mission planing, and just simply working around this limitation.

Overall, the results demonstrate that sliding mode control enables magnetorquer only attitude control to meet ICARUS pointing requirements under both static and dynamic conditions, at the expense of increased power consumption compared to the classical PD approach.

Chapter 6

Conclusion

This thesis addressed the design and numerical validation of a magnetorquer only attitude control system for the ICARUS 1U CubeSat. The primary objective was to determine whether the mission pointing requirement of maintaining the Langmuir probe within ±10° of the ram direction could be achieved using exclusively magnetic actuation while respecting the stringent mass, volume, power, and computational constraints of a CubeSat platform.

To achieve this objective, the spacecraft attitude dynamics were formulated in quaternion error coordinates and adapted to the specific characteristics of magnetic actuation. A nonlinear sliding mode controller was implemented and compared against a classical quaternion based PD controller within a high fidelity MATLAB simulation environment incorporating orbital propagation, geomagnetic field modeling, spacecraft rotational dynamics, and Monte Carlo performance evaluation.

The simulation results demonstrate that the proposed sliding mode controller consistently satisfies the ICARUS pointing requirement under both static and dynamic pointing scenarios. Average pointing errors remained close to 5°, while the classical PD controller exhibited steady-state errors exceeding 20° under identical conditions. These results confirm that explicitly accounting for the nonlinear and time varying characteristics of magnetic actuation substantially improves pointing performance without increasing algorithmic complexity beyond what is suitable for embedded implementation.

The study also highlights the inherent trade offs associated with purely magnetic attitude control. Although the sliding mode controller provides significantly better pointing accuracy and robustness, this improvement is accompanied by increased magnetorquer power consumption. Nevertheless, the obtained performance suggests that the additional energy expenditure is acceptable for scientific operations, provided that mission planning accounts for the spacecraft power budget and eclipse periods.

It should be noted that the presented results correspond to an idealized simulation environment. Several effects, including sensor estimation errors, battery state evolution, and additional environmental disturbances, were either simplified or neglected to maintain reasonable simulation complexity. Consequently, while the results provide strong evidence of the controller's effectiveness, experimental validation and higher-fidelity modeling remain necessary before flight deployment.

Future work should therefore focus on extending the simulation framework to include complete ADCS sensor models, realistic state estimation algorithms, and more detailed environmental disturbance models. Hardware implementation on the ICARUS ADCS electronics, followed by hardware-in-the-loop testing, will provide an important intermediate validation step before in-orbit operation.

Overall, this work demonstrates that magnetorquer only attitude control is capable of meeting the pointing requirements of the ICARUS mission when an appropriate nonlinear control strategy is employed. Beyond providing a validated control solution for ICARUS, the proposed framework contributes to the broader development of robust and computationally efficient attitude control systems for future low cost CubeSat missions requiring moderate pointing accuracy.

References

[1] *Porto space team*, portospaceteam.pt. [Online]. Available: https://www.portospaceteam.pt/pt.

[2] M. Y. Ovchinnikov and D. S. Roldugin, *A survey on active magnetic attitude control algorithms for small satellites*, 2019. DOI: 10.1016/j.paerosci.2019.05.006.

[3] S. P. Bhat, "Controllability of nonlinear time-varying systems: Applications to spacecraft attitude control using magnetic actuation," *IEEE Transactions on Automatic Control*, vol. 50, 11 2005, ISSN: 00189286. DOI: 10.1109/TAC.2005.858686.

[4] H. Hoang et al., "The multi-needle langmuir probe system on board NorSat-1," *Space Science Reviews*, vol. 214, no. 4, p. 75, May 8, 2018, ISSN: 1572-9672. DOI: 10.1007/s11214-018-0509-2. Accessed: Dec. 30, 2024. [Online]. Available: https://doi.org/10.1007/s11214-018-0509-2.

[5] T. A. Bekkeng, E. S. Helgeby, A. Pedersen, E. Trondsen, T. Lindem, and J. I. Moen, "Multi-needle langmuir probe system for electron density measurements and active spacecraft potential control on CubeSats," *IEEE Transactions on Aerospace and Electronic Systems*, vol. 55, no. 6, pp. 2951–2964, Dec. 2019, Conference Name: IEEE Transactions on Aerospace and Electronic Systems, ISSN: 1557-9603. DOI: 10.1109/TAES.2019.2900132. Accessed: Dec. 30, 2024. [Online]. Available: https://ieeexplore.ieee.org/document/8643865/?arnumber=8643865.

[6] S. Marholm, R. Marchand, D. Darian, W. J. Miloch, and M. Mortensen, "Impact of miniaturized fixed-bias multineedle langmuir probes on CubeSats," *IEEE Transactions on Plasma Science*, vol. 47, no. 8, pp. 3658–3666, Aug. 2019, Conference Name: IEEE Transactions on Plasma Science, ISSN: 1939-9375. DOI: 10.1109/TPS.2019.2915810. Accessed: Dec. 30, 2024. [Online]. Available: https://ieeexplore.ieee.org/document/8734022/?arnumber=8734022.

[7] K. S. Jacobsen, A. Pedersen, J. I. Moen, and T. A. Bekkeng, "A new langmuir probe concept for rapid sampling of space plasma electron density," *Measurement Science and Technology*, vol. 21, no. 8, p. 085 902, Jul. 2010, ISSN: 0957-0233. DOI: 10.1088/0957-0233/21/8/085902. Accessed: Dec. 30, 2024. [Online]. Available: https://dx.doi.org/10.1088/0957-0233/21/8/085902.

[8] A. Phanse et al., "Design, implementation and comparison of power electronic circuits for current control through 3-axis magnetorquer coils in a satellite," in *2019 IEEE 13th International Conference on Power Electronics and Drive Systems (PEDS)*, 2019, pp. 1–6. DOI: 10.1109/PEDS44367.2019.8998925.

[9] M. Musaib, A. Dildar, A. Ali, and H. Ali, "Embedded magnetorquer coil design for microsatellite," Tech. Rep., 2016. [Online]. Available: https://www.researchgate.net/publication/341100030.

[10] H. Curtis, *Orbital Mechanics for Engineering Students: Revised Reprint*. 2020. DOI: 10.1016/B978-0-12-824025-0.09973-6.

[11] Wikipedia contributors, *Orbital elements — Wikipedia, the free encyclopedia*, [Online; accessed 6-January-2026], 2026. [Online]. Available: https://en.wikipedia.org/w/index.php?title=Orbital_elements&oldid=1363213323.

[12] D. Vallado, P. Crawford, R. Hujsak, and T. Kelso, "Revisiting spacetrack report 3: Rev," Aug. 2006.

[13] S. Aida and M. Kirschner, "Accuracy assessment of sgp4 orbit information conversion into osculating elements," Apr. 2013.

[14] J. J. Z. J. Sanz Subirana and S. M. Hernández-Pajares Technical University of Catalonia, *Conventional celestial reference system*, [Online; accessed 5-January-2026], 2011. [Online]. Available: https://gssc.esa.int/navipedia/index.php?title=Conventional_Celestial_Reference_System.

[15] Godard, K. D. Kumar, and A.-M. Zou, "A novel single thruster control strategy for spacecraft attitude stabilization," *Acta Astronautica*, vol. 86, pp. 55–67, 2013, ISSN: 0094-5765. DOI: https://doi.org/10.1016/j.actaastro.2012.12.018. [Online]. Available: https://www.sciencedirect.com/science/article/pii/S0094576512004985.

[16] F. L. Markley and J. L. Crassidis, *Fundamentals of spacecraft attitude determination and control*. 2014. DOI: 10.1007/978-1-4939-0802-8.

[17] *Modern Spacecraft Guidance, Navigation, and Control*. 2023. DOI: 10.1016/c2020-0-03563-2.

[18] M. Ovchinnikov, V. Pen'kov, O. Norberg, and S. Barabash, "Attitude control system for the first swedish nanosatellite 'munin'," *Acta Astronautica*, vol. 46, 2 2000, ISSN: 00945765. DOI: 10.1016/S0094-5765(99)00226-X.

[19] L. H. GRASSHOFF, "A method for controlling the attitude of a spin-stabilized satellite," *ARS Journal*, vol. 31, 5 1961. DOI: 10.2514/8.5589.

[20] G. Avanzini, E. L. de Angelis, F. Giulietti, and N. Serrano, "Attitude control of low earth orbit satellites by reaction wheels and magnetic torquers," *Acta Astronautica*, vol. 160, 2019, ISSN: 00945765. DOI: 10.1016/j.actaastro.2019.03.013.

[21] S. A. khan, Y. Shiyou, A. Ali, M. Tahir, S. Fahad, and S. Rao, "Cubesats detumbling using only embedded asymmetric magnetorquers," *Advances in Space Research*, vol. 71, 5 2023, ISSN: 18791948. DOI: 10.1016/j.asr.2022.10.053.

[22] M. A. Desouky and O. Abdelkhalik, "A new variant of the b-dot control for spacecraft magnetic detumbling," *Acta Astronautica*, vol. 171, 2020, ISSN: 00945765. DOI: 10.1016/j.actaastro.2020.02.030.

[23] N. Petit and I. Sarras, "A generalized control law for uniform, global and exponential magnetic detumbling of rigid spacecraft," in *IFAC-PapersOnLine*, vol. 53, 2020. DOI: 10.1016/j.ifacol.2020.12.1946.

[24] M. Lovera and A. Astolfi, "Spacecraft attitude control using magnetic actuators," *Automatica*, vol. 40, 8 2004, ISSN: 00051098. DOI: 10.1016/j.automatica.2004.02.022.

[25] M. Reyhanoglu, C. Ton, and S. Drakunov, “Attitude stabilization of a nadir-pointing small satellite using only magnetic actuators,” *IFAC Proceedings Volumes*, vol. 42, no. 19, pp. 292–297, 2009, 2nd IFAC Conference on Intelligent Control Systems and Signal Processing, ISSN: 1474-6670. DOI: https://doi.org/10.3182/20090921-3-TR-3005.00052. [Online]. Available: https://www.sciencedirect.com/science/article/pii/S1474667015308491.

[26] A. Sofyalı, E. M. Jafarov, and R. Wisniewski, “Robust and global attitude stabilization of magnetically actuated spacecraft through sliding mode,” *Aerospace Science and Technology*, vol. 76, 2018, ISSN: 12709638. DOI: 10.1016/j.ast.2018.01.022.

[27] M. Y. Ovchinnikov, D. S. Roldugin, V. I. Penkov, S. S. Tkachev, and Y. V. Mashtakov, “Fully magnetic sliding mode control for acquiring three-axis attitude,” *Acta Astronautica*, vol. 121, 2016, ISSN: 00945765. DOI: 10.1016/j.actaastro.2015.12.031.

[28] X. Chen and X. Wu, “Model predictive control of cube satellite with magneto-torquers,” in *2010 IEEE International Conference on Information and Automation, ICIA 2010*, 2010. DOI: 10.1109/ICINFA.2010.5512149.

[29] T. Huang, J. Zhang, M. Li, Y. Shen, J. Wu, and H. Wang, “Self-triggered mpc with adaptive prediction horizon for nano-satellite attitude control system,” *Advances in Space Research*, vol. 75, 2 2025, ISSN: 18791948. DOI: 10.1016/j.asr.2024.10.022.

[30] R. Wiśniewski, “Linear time-varying approach to satellite attitude control using only electromagnetic actuation,” *Journal of Guidance, Control, and Dynamics*, vol. 23, 4 2000, ISSN: 07315090. DOI: 10.2514/2.4609.

[31] M. L. Psiaki, “Magnetic torquer attitude control via asymptotic periodic linear quadratic regulation,” *Journal of Guidance, Control, and Dynamics*, vol. 24, 2 2001, ISSN: 15333884. DOI: 10.2514/2.4723.

[32] M. F. Shehzad, A. B. Asghar, M. H. Jaffery, K. Naveed, and Z. Čonka, “Neuro-fuzzy system based proportional derivative gain optimized attitude control of cubesat under leo perturbations,” *Heliyon*, vol. 9, 10 2023, ISSN: 24058440. DOI: 10.1016/j.heliyon.2023.e20434.

[33] G. Avanzini and F. Giulietti, “Magnetic detumbling of a rigid spacecraft,” *Journal of Guidance, Control, and Dynamics*, vol. 35, no. 4, pp. 1326–1334, 2012. DOI: 10.2514/1.53074. eprint: https://doi.org/10.2514/1.53074. [Online]. Available: https://doi.org/10.2514/1.53074.

[34] F. L. Markley, Y. Cheng, J. L. Crassidis, and Y. Oshman, “Averaging quaternions,” *Journal of Guidance, Control, and Dynamics*, vol. 30, no. 4, pp. 1193–1197, 2007. DOI: 10.2514/1.28949. eprint: https://doi.org/10.2514/1.28949. [Online]. Available: https://doi.org/10.2514/1.28949.